

# Advances in Nanoparticle-Enhanced Thermoelectric Materials from Synthesis to Energy Harvesting: A Review

Wajid Hussain, Salem Algarni, Ghulam Rasool,\* Hasan Shahzad, Mujahid Abbas, Talal Alqahtani, and Kashif Irshad

Cite This: *ACS Omega* 2024, 9, 11081–11109

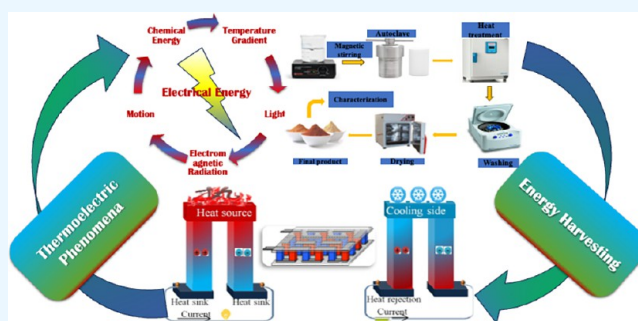
Read Online

ACCESS |

Metrics & More

Article Recommendations

**ABSTRACT:** This comprehensive review analysis examines the domain of composite thermoelectric materials that integrate nanoparticles, providing a critical assessment of their methods for improving thermoelectric properties and the procedures used for their fabrication. This study examines several approaches to enhance power factor and lattice thermal conductivity, emphasizing the influence of secondary phases and structural alterations. This study investigates the impact of synthesis methods on the electrical characteristics of materials, with a particular focus on novel techniques such as electrodeposition onto carbon nanotubes. The acquired insights provide useful guidance for the creation of new thermoelectric materials. The review also compares and contrasts organic and inorganic thermoelectric materials, with a particular focus on the potential of inorganic materials in the context of waste heat recovery and power production within industries. This analysis highlights the role of inorganic materials in improving energy efficiency and promoting environmental sustainability.



## 1. INTRODUCTION

Thermoelectric materials, an intriguing category of materials<sup>1</sup> possessing the distinctive capability to directly convert thermal energy into electrical energy and vice versa,<sup>2</sup> have attracted considerable attention due to their potential in tackling energy-related issues.<sup>3</sup> This introduction presents a comprehensive overview regarding the basic principles of thermoelectricity, and we will discuss the specific characteristics of thermoelectric materials, their historical development, and their various uses. Furthermore, an examination of current progress and prospective developments in this captivating domain are undertaken, with a particular emphasis on the potential of thermoelectric materials to make significant contributions to the realm of sustainable energy solutions.<sup>4</sup> The thermoelectric effect, which encompasses the Seebeck effect, the Peltier effect, and the Thomson effect, serves as the fundamental basis of thermoelectricity, facilitating the direct conversion of heat energy into electrical energy.<sup>5</sup> The Seebeck effect is accountable for the production of an electric potential difference across a thermal gradient, enabling the conversion of thermal energy into electrical energy.<sup>6</sup> On the other hand, the Peltier effect entails the absorption or release of heat at the interface of two dissimilar materials when an electric current is applied, thereby facilitating the development of devices for heating or cooling purposes.<sup>7</sup> The Thomson effect, however, is associated with the temperature gradient observed in a

conductor that carries an electric current, leading to the generation or absorption of heat.<sup>8</sup> The quantification of thermoelectric material efficiency is reliant upon a crucial metric known as the figure-of-merit ( $ZT$ ), which is impacted by the characteristics of electrical conductivity, Seebeck coefficient, and thermal conductivity. The adjustment of these parameters plays a critical role in attaining greater  $ZT$  values, hence enhancing energy conversion efficiency.<sup>9</sup> In order to get maximum efficiency in thermoelectric materials, it is essential to possess a comprehensive understanding of their inherent properties and prerequisites. These include but are not limited to high electrical conductivity, low thermal conductivity, and suitable electronic band structures.<sup>10</sup> Various categories of materials, including inorganic and organic materials, possess distinct characteristics that have an impact on their thermoelectric efficiency.<sup>11</sup> The origins of thermoelectric materials can be attributed to the early 19th century, during which the scientific community's inquisitiveness led to the identification of the Seebeck effect by Thomas Seebeck.<sup>12</sup>

**Received:** October 6, 2023  
**Revised:** February 10, 2024  
**Accepted:** February 20, 2024  
**Published:** February 29, 2024



Over the course of time, scholars have achieved notable advancements in the enhancement of materials and devices, resulting in the contemporary utilization of thermoelectric materials in several domains such as waste heat retrieval, power production, space exploration, and portable electronic gadgets, among other areas.<sup>13</sup> The field of materials science and nanotechnology has witnessed significant progress in recent times, leading to the emergence of novel opportunities for improving the capabilities of thermoelectric materials.<sup>14</sup> The researchers have made significant findings in the field of materials science by identifying new materials that exhibit enhanced thermoelectric properties. They have also employed nanostructuring methods to effectively decrease thermal conductivity. Furthermore, innovative computational modeling techniques have been employed to accurately forecast and enhance the performance of these materials. In light of the urgent energy and environmental difficulties that the world currently confronts, thermoelectric materials possess significant potential in effectively tackling these concerns.<sup>15</sup> The incorporation of thermoelectric materials into expansive power generation systems and harnessing renewable energy sources can significantly contribute to the advancement of sustainable energy solutions. Nevertheless, there exist certain obstacles that must be surmounted, including the enhancement of materials' efficiency and stability, the reduction of production expenses, and the mitigation of the environmental repercussions associated with thermoelectric devices.<sup>16</sup> The exertion of endeavors in the expansive domains of thermoelectric materials will undoubtedly prove imperative for unlocking the full spectrum of their capabilities in practical applications.<sup>17</sup> As we embark on this journey, it becomes increasingly evident that a comprehensive understanding and harnessing of thermoelectric materials hold the key to transformative advancements across diverse sectors, ushering in a more sustainable trajectory for the future of energy utilization.<sup>18</sup> At the core of this pursuit lies the intrinsic potential of thermoelectric materials for efficient energy conversion and the reclamation of waste heat. Their unique ability to directly convert heat into electricity opens up a myriad of possibilities for utilization in various industries.<sup>19</sup> This potentiality not only addresses the growing energy demands but also addresses the pressing concern of waste heat, offering an innovative solution to mitigate environmental impacts.<sup>20</sup> The imperative now is to delve deeper into these materials, explore their nuances, and refine their applications for optimal performance. Scholarly inquiry stands as the cornerstone of progress in this realm.<sup>21</sup> The persistent exploration of thermoelectric materials through rigorous research endeavors is essential for unraveling the complexities and unlocking their full potential.<sup>22</sup> If investigators and scientists throughout the globe want to comprehend these materials in their entirety, they will need to work together in an interdisciplinary fashion, combining their knowledge of materials science with that of physics and engineering. This collaborative approach will enable the identification of novel materials with enhanced thermoelectric properties and the development of innovative techniques for their fabrication. Technological advancements play a pivotal role in bridging the gap between theoretical potential and practical application.<sup>23</sup> Cutting-edge innovations in manufacturing processes, material design, and device engineering are essential for realizing the promise of thermoelectric materials on a large scale. Moreover, the integration of these materials into existing infrastructures

and the development of new, efficient systems are critical steps toward their extensive incorporation across diverse sectors.<sup>24</sup> Thermoelectric materials hold significant potential for energy conversion and the retrieval of waste heat, as their ability to directly convert heat into electricity presents a wide range of possibilities for utilization in various industries. By means of persistent scholarly inquiry, progressive technological developments, and concerted cooperative endeavors, the capacity of thermoelectric materials can be further investigated and augmented, hence facilitating the realization of a more environmentally sustainable and energetically efficient global landscape.

**1.1. Seebeck Effect.** During the period of 1821–1823, Thomas Johann Seebeck conducted an experiment in which he observed that the introduction of a circuit including two metals of differing compositions, with junctions exposed to varying temperatures, resulted in the deflection of a compass magnet.<sup>25</sup> Initially, Seebeck postulated that this phenomenon was attributable to magnetism caused by the disparity in temperature and speculated that it could potentially be associated with the magnetic field of the Earth. Nevertheless, it was promptly recognized that the application of a “Thermoelectric Force” resulted in the generation of an electric current, which, in accordance with Ampere’s law, causes the magnet to experience deflection. To be more precise, the disparity in temperature gives rise to an electrical potential (voltage) that has the capability to induce an electric current within a complete circuit. Presently, this phenomenon is recognized as the Seebeck effect. Seebeck employed an apparatus to detect the deviation of a magnetic needle (a) caused by a thermoelectrically produced current resulting from the heating of the interface between two dissimilar metals (n and o). The voltage created is exactly proportional to the temperature difference between the two junctions. The Seebeck coefficient, represented as  $S$  or  $a$ , is a constant of proportionality that is generally known as the thermo power, although it is primarily linked to potential rather than power. Gustav Magnus made a discovery in 1851 which showed that the Seebeck voltage remains constant regardless of the temperature distribution along the metal connections between the junctions. This discovery implies that the thermo power may be regarded as a thermodynamic state function.<sup>26</sup> The physical foundation behind the operation of a thermocouple, a widely employed device for temperature detection, is hereby elucidated. Seebeck conducted a comprehensive survey encompassing a wide range of materials, including elements, alloys, and minerals. The materials examined included zinc antimonide, chalcogenide minerals such as lead sulfide (PbS), and cobalt arsenide. Through this investigation, Seebeck established a qualitative ranking of these materials based on their respective Seebeck effect. In 1910, Werner Haken conducted a quantitative analysis of the Seebeck coefficient (measured in microvolts per Kelvin) and electrical conductivity of various elements, alloys, and compounds. Haken’s work built upon the earlier studies conducted by Becquerel on ZnSb and CdSb.<sup>27</sup> Notably, Haken correctly identified Sb<sub>2</sub>Te<sub>3</sub>, Bi<sub>2</sub>Te<sub>3</sub>, Bi<sub>0.9</sub>Sb<sub>0.1</sub>, SnTe, and Cu–Ni alloys as promising thermoelectric materials. Additionally, Haken conducted a study on PbTe.<sup>28</sup> In the subsequent two decades, William Thomson, who would later be recognized as Lord Kelvin, provided a thorough elucidation of the Seebeck and Peltier Effects, offering a detailed account of their interconnection, commonly referred to as the Kelvin Relations.<sup>29</sup> The relationship between the Seebeck and Peltier

coefficients is established within the framework of thermodynamics. The Peltier coefficient can be defined as the product of the Seebeck coefficient and the absolute temperature. The derivation of thermodynamics conducted by Thomson resulted in the anticipation of a third thermoelectric phenomenon, which is presently referred to as the Thomson effect. The Thomson effect refers to the phenomenon where the flow of electric current through a substance with a temperature gradient results in the absorption or production of heat. The relationship between heat and both electric current and temperature gradient is one of proportionality. The Thomson coefficient, which serves as the proportionality constant, is thermodynamically linked to the Seebeck coefficient. The utilization of the constant property model for determining the maximum efficiency of a thermoelectric generator and the performance of a cooler was pioneered by Edmund Altenkirch in 1909 and 1911, respectively. These calculations were conducted under the assumption that the design and operating parameters were fully optimized.<sup>30</sup> The aforementioned correlation eventually evolved into the concept of the “figure-of-merit”  $ZT$ , which stipulates that thermoelectric materials of high quality should exhibit substantial Seebeck coefficients, elevated electrical conductivity (in order to mitigate Joule heating caused by electrical resistance), and reduced thermal conductivity (to decrease heat dissipation). The initial investigations conducted by A. Eucken<sup>31</sup> about thermal conductivity in solids expeditiously demonstrated that the presence of point defects in alloys substantially diminishes the lattice thermal conductivity. This observation underscores the significance of this approach in the development of thermoelectric materials.

**1.2. Properties of Materials Relating to Their Thermoelectricity.** The ability of a thermoelectric material to effectively convert heat into electricity is directly proportional to the performance of the thermoelectric device (whether it be used for power generating or cooling). The efficacy of a thermoelectric material is primarily governed by its figure-of-merit, represented by the symbol  $ZT$ .<sup>32</sup>

$$ZT = S^2 \sigma T / \kappa \text{ or } ZT = \frac{\alpha^2}{\rho k} T \quad (1)$$

The generation of voltage is facilitated by the Seebeck coefficient, denoted as  $S$  or  $\alpha$ . Furthermore, achieving high efficiency necessitates the presence of a low electrical resistivity  $\rho$  (or conversely, a high electrical conductivity  $\sigma$ ) as well as a low thermal conductivity  $\kappa$ . The  $zT$  values of many commonly utilized materials in commercial applications, NASA missions, and verified in laboratory settings are presented in the following table.<sup>33</sup> These values serve as a valuable reference point for the enhancement of materials. Several studies have shown the existence of numerous materials exhibiting higher thermoelectric figure-of-merit ( $zT$ ), indicating significant progress in this sector. However, it is important to acknowledge the potential challenges related to stability and measurement, as highlighted in ref 34. In order to get an adequate power output, it is imperative to employ a thermoelectric (TE) generator with optimal efficiency over a substantial temperature differential  $\Delta T = T_H - T_C$ . Consequently, the material's thermoelectric figure-of-merit ( $zT$ ) must exhibit good performance across this specific temperature span. The device  $ZT$  refers to a weighted average of the TE material  $zT$ , which is determined by maximizing the efficiency  $\eta$  within a given

temperature difference  $\Delta T$ . This calculation may be readily performed using the material characteristics  $S$ ,  $\rho$ , and  $\kappa$ .

$$\eta_{\max} = \frac{T_H - T_C}{T_H} \frac{\sqrt{1 + zT} - 1}{\sqrt{1 + zT} + \frac{T_C}{T_H}} \quad (2)$$

Here, we write  $T_H$  for the temperature at the hot thermoelectric junction and  $T_C$  for the temperature at the cold thermoelectric junction. Extensive research and development have gone into determining the figure-of-merit of thermoelectric materials. Here we see novel approaches that seek to enhance thermoelectric materials and boost energy conversion efficiency. The following are instances of such enhanced characteristics: resonant states, anharmonicity, band convergence, “phonon-glass electron-crystal”, multiscale phonon scattering, etc. These concepts have led to the discovery of several novel thermoelectric materials with intriguing features, including atom-rattling cages, nanostructures of varied sizes, solids with high band degeneracy, and many more. The function shows that improving one or more factors independently to increase the  $zT$  seems to be a simple task. However, due to the many contradictory interactions among the different attributes, matters become more complicated. In order to include the related aspects into the optimization problem overall, more decoupling or extra degrees of freedom are obviously required. Electrical and thermal transport optimization must occur simultaneously.

## 2. REVIEW OF RELATED LITERATURE

**2.1. Materials Based on Cuprous Selenide (Cu<sub>2</sub>Se) for Thermoelectric Use.** In a study conducted by Wang-Wei Liao et al. in 2019, the researchers emphasize the potential of  $\alpha$ -Cu<sub>2</sub>Se as a thermoelectric material with promising applications at near-room temperatures. The authors achieved this by incorporating bismuth into the material, which resulted in a reduction in carrier concentration. This drop resulted in a significant enhancement in the power factor and a reduction in carrier thermal conductivity. The researchers achieved a figure-of-merit ( $zT$ ) value of 0.43 at a temperature of 373 K in the specific composition of Cu<sub>1.982</sub>Bi<sub>0.006</sub>Se.<sup>35</sup> The authors, Liu et al., drew attention to the significance of Cu<sub>2</sub>X (X = Te, Se, and S) thermoelectric materials in terms of their liquid-like characteristics and high figure-of-merit. They provide an overview of effective approaches for enhancing performance and delve into discussions regarding stabilities, mechanical properties, and potential avenues for improving energy conversion efficiency. This information is documented in ref 36. The study conducted by Jin et al. examines the impact of Ag on the thermoelectric properties and durability of Cu<sub>2</sub>Se samples. The findings indicate that Cu<sub>2</sub>Se materials containing Ag exhibit enhanced thermoelectric properties while maintaining stability. Consequently, the authors suggest the adoption of a rational leg geometry for Cu<sub>1.97</sub>Ag<sub>0.03</sub>Se-based thermoelectric modules to achieve both stability and efficiency.<sup>37</sup> In their study published in 2021, Yang et al. introduced a novel approach for synthesizing Cu<sub>2</sub>Se-based materials with excellent thermoelectric properties. This method involves the application of a pulse electric current, which is both efficient and cost-effective. The scientists stabilized dynamic Cu-ion fluctuation zones by using the pinning action of dislocations and interfacial/border phases, which resulted in the construction of a hierarchical structure. This hierarchical structure greatly improves the thermoelectric materials based on

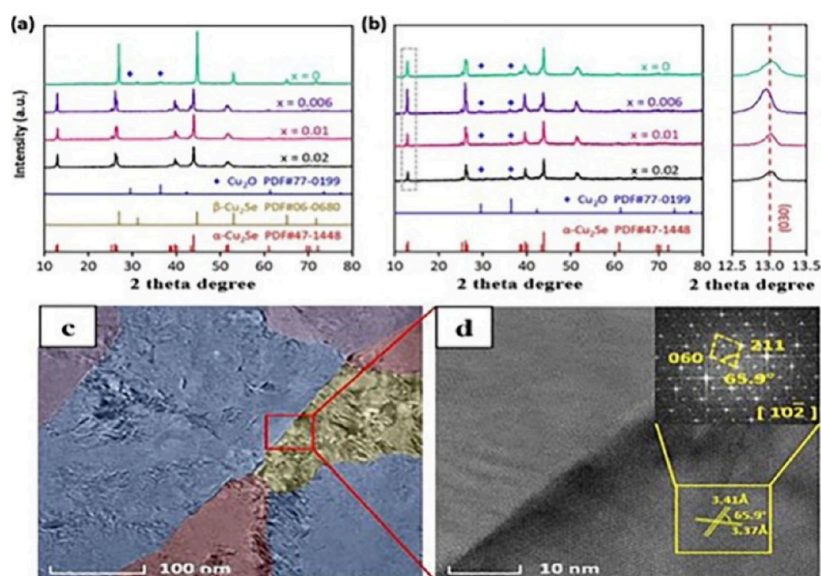


**Figure 1.** (a) XRD results of  $\text{Cu}_2-3x\text{Bi}_x\text{Se}$  ( $x = 0, 0.006, 0.01, 0.02$ ) powder samples and (b) bulk samples (the inset shows the 030 peaks for all samples). (c) TEM image of bulk  $\text{Cu}_{1.982}\text{Bi}_{0.006}\text{Se}$ . (d) High-resolution TEM (HRTEM) image of the square area.<sup>27</sup> Copyright ACS Applied Energy Materials 2022, 5, 7913–7943.

$\text{Cu}_2\text{Se}$ 's stability, thereby improving their overall performance.<sup>38</sup> In their 2021 study, Choo et al. present a proposal for enhancing the efficiency and longevity of power generation through cellular thermoelectric architectures. They achieve this by utilizing  $\text{Cu}_2\text{Se}$  thermoelectric materials and employing extrusion-based 3D printing techniques. The authors optimize the aspect ratio and introduce a mechanically rigid hollow hexagonal column and honeycomb-based thermoelectric legs. Additionally, they incorporate  $\text{Cu}_2\text{Se}$ -based 3D-printing inks that do not require the use of organic binders.<sup>39</sup> In a study conducted by Li et al. in 2022, a novel approach was employed to incorporate  $\text{Cu}_2\text{Se}$  into  $\text{AgCuTe}$ , resulting in the formation of multilayered nanostructures. This innovative technique led to a significant reduction in thermal conductivity, achieving the lowest recorded value of approximately  $0.45 \text{ W m}^{-1} \text{ K}^{-1}$  at a temperature of 723 K. Consequently, the average ZT value between 523 and 723 K reached approximately 1.13, surpassing the average performance of previously published materials based on  $\text{AgCuTe}$ . These findings highlight the potential for further advancements in thermoelectric capabilities.<sup>40</sup> In a study conducted by Nieroda et al. in 2022, the sintering process of  $\text{Cu}_2\text{S}$  and  $\text{Cu}_2\text{Se}$  powders was investigated using a Spark Plasma Sintering (SPS) apparatus. The SPS apparatus was equipped with both direct current (DC) and alternating current (AC) power sources. The findings of the study demonstrated that the utilization of AC current in the sintering process can retain the benefits of SPS while mitigating the deterioration of superionic thermoelectric materials. Consequently, this approach proves to be more suitable for sintering various super ionic materials.<sup>41</sup> In a study conducted by Rudradawong et al. in 2023, it was shown that the substitution of Sb on Se sites in  $\text{Cu}_2\text{Se}$  thermoelectric materials leads to an important development in their performance. The highest achievable figure of excellence (ZT) value was 0.47 at a temperature of 523 K, attained by a doping level of  $x = 0.005$ .<sup>42</sup> In a study conducted by Mangavati et al. in 2023, the researchers examined the characteristics of  $\text{Cu}_2\text{Se}/\text{Y}_2\text{O}_3$  composites with varying concentrations of  $\text{Y}_2\text{O}_3$ . The results demonstrated the

successful integration of  $\text{Y}_2\text{O}_3$  into the composites, leading to an enhancement in mechanical hardness and thermal conductivity. However, there was a decrease observed in the power factor and ZT values, indicating the influence of  $\text{Y}_2\text{O}_3$  addition on the thermoelectric properties of  $\text{Cu}_2\text{Se}$ -based materials.<sup>43</sup> In their study published in 2023, Bhat et al. examined the impact of Bi doping on the mechanical and thermoelectric characteristics of  $\text{Cu}_2\text{Se}$ . The sample with a composition of  $\text{Cu}_{1.988}\text{Bi}_{0.012}\text{Se}$  demonstrates the most noteworthy power factor of  $1474 \mu\text{W m}^{-1} \text{ K}^{-2}$  at 700 K, suggesting its promising prospects as a thermoelectric material with high performance. This finding is supported by the corresponding ZT value.<sup>44</sup> The authors of the study are Zhao and Huijuan et al. The study was published in 2023. The use of high-resolution microscopy reveals a well-defined and fully enclosed binary-sublattice structure inside  $\alpha\text{-Cu}_2\text{Se}$ . This configuration maintains optimal electron transport efficiency while enhancing phonon scattering. These findings provide insight into methods for improving the thermoelectric performance of materials in future designs.<sup>45</sup> In 2023, Zhi et al. discovered that by doping  $\text{Cu}_2\text{Se}$  with S and Te the material's electronic band structure becomes more aligned, resulting in improved carrier mobility and power factor. Additionally, the presence of scattered second-phase features, dislocations, and nanograins further enhances its performance. As a result, the material achieves an impressive zT value of 2.34 at 850 K, exceeding the performance of pure  $\text{Cu}_2\text{Se}$ .<sup>46</sup> Xiaomeng et al. in the year 2023 found that enhancing the electrical transport characteristics and perhaps boosting the efficiency of p-type thermoelectric materials may be achieved by manipulating the band structure of  $\text{Cu}_2\text{Se}$  by the introduction of effective dopants such as Fe or Mn substitutional defects and copper vacancies. This enhances the degeneracy of the valence band and resolves the issue of its reduced power factor. This hypothesis is substantiated by first-principles calculations.<sup>47</sup>

The X-ray diffraction (XRD) patterns seen in Figure 1(a) demonstrate the occurrence of phase transitions when Bi doping is introduced into  $\text{Cu}_2-3x\text{Bi}_x\text{Se}$ . These findings are

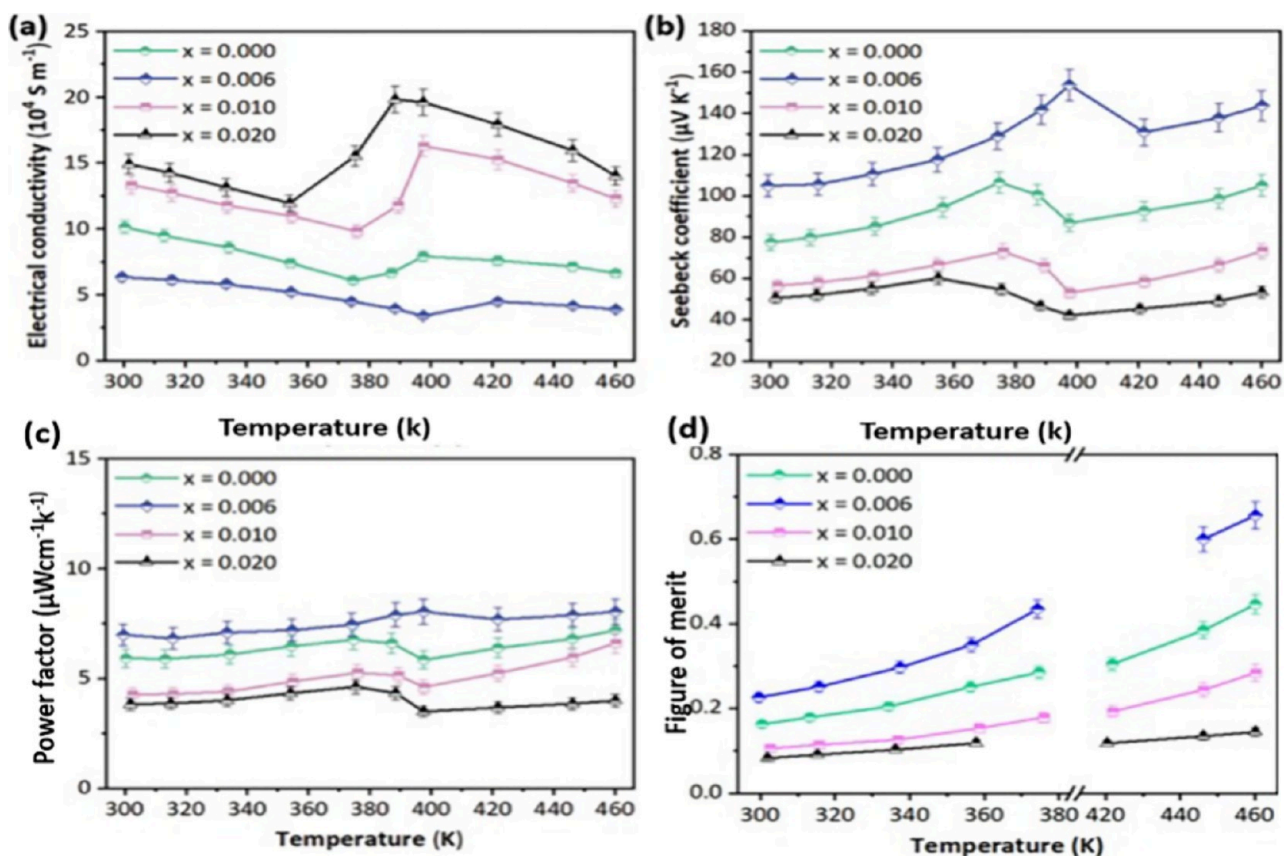


**Figure 2.** Illustration of the temperature-dependent electrical transport properties of  $\text{Cu}_2-3x\text{Bi}_x\text{Se}$  ( $x = 0, 0.006, 0.01, 0.02$ ): (a) electrical conductivity ( $\sigma$ ), (b) Seebeck coefficient ( $S$ ), (c) power factor, and (d) the figure-of-merit  $ZT$ .<sup>27</sup> Copyright ACS Applied Energy Materials 2022, 5, 7913–7943.

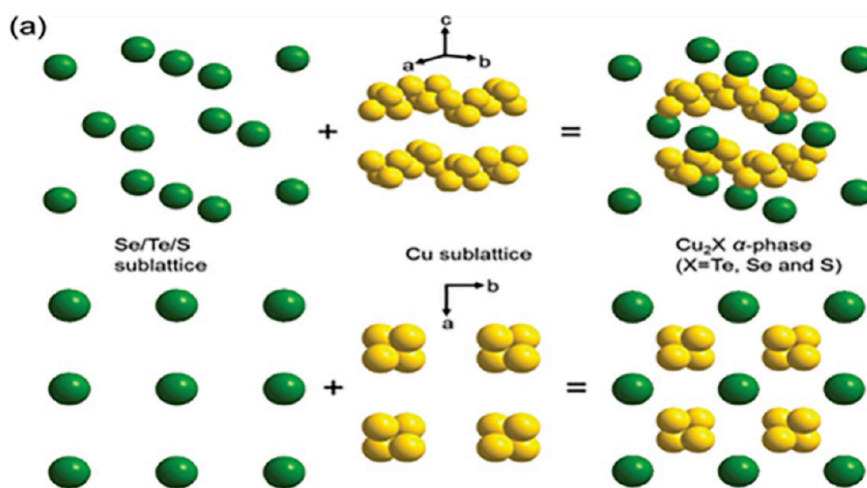


**Figure 3.** Schematic diagram of the crystal structure of  $\text{Cu}_2\text{Se}$  and  $\text{CuS}$ .<sup>28</sup> Copyright Advanced Materials 2020, 32, 1–28.

consistent with prior investigations on nanostructured  $\text{Cu}_2\text{Se}$ . The sintered samples, as shown in Figure 1(b), exhibit the retention of the  $\alpha\text{-Cu}_2\text{Se}$  phase after the Spark Plasma Sintering (SPS) process, suggesting little alteration in size. Transmission electron microscopy (TEM) investigation was conducted on sintered  $\text{Cu}_{1.982}\text{Bi}_{0.006}\text{Se}$ , as shown in Figure 1(c). The study revealed the presence of nanoscale grains. Furthermore, high-resolution TEM (HRTEM) imaging, as shown in Figure 1(d), provided confirmation of successful Bi doping by observing changes in lattice spacing.

Figure 2 depicts the focus of the study, which centers on the examination of the electrical transport properties of  $\text{Cu}_2-3x\text{Bi}_x\text{Se}$ , with  $x$  representing several values including 0, 0.006, 0.01, and 0.02, as a function of temperature. The present study evaluates various important parameters, such as electrical conductivity ( $\sigma$ ), which quantifies the material's capability to conduct electric current; Seebeck coefficient ( $S$ ), which indicates its ability to generate voltage based on temperature disparities; power factor, the multiplication of  $S$  and  $\sigma$ , which emphasizes its efficiency in converting thermal energy into

electricity; and the figure-of-merit (ZT), a comprehensive parameter that evaluates the overall thermoelectric performance of the material. The present research offers valuable insights into the potential of the material for applications that need the conversion of heat into electricity in an effective manner.<sup>27</sup>

The schematic of Figure 3 depicts the crystal structure of  $\alpha$ -Cu<sub>2</sub>X (where X represents Te, Se, and S) phases and provides a visual representation of the spatial organization of atoms inside the lattice. The compounds under consideration exhibit a cubic-close-packed (ccp) configuration, whereby copper (Cu) atoms provide the foundation of the lattice structure. The chalcogen (X) atoms are positioned around each copper atom, occupying the octahedral positions located between the copper atoms. The  $\alpha$ -Cu<sub>2</sub>X structure exhibits a coordination of six chalcogen atoms around each copper atom, resulting in the formation of a three-dimensional network. The chalcogen atoms form chemical interactions with adjacent copper atoms, forming strong interatomic connections within the lattice structure. The aforementioned configuration leads to the distinctive attributes of the compound, including its electrical and thermal characteristics. The structure of  $\alpha$ -Cu<sub>2</sub>X has a distinct symmetry that has a significant impact on its characteristics. The crystal structure of copper is characterized by a cubic-close-packed arrangement of its atoms, which exhibits a repetitive pattern across the lattice, leading to a highly organized and orderly structure.

The aforementioned regularity plays a significant role in shaping the electronic band structure of the material and has a direct impact on its electrical and thermal conductivity. The schematic figure offers valuable information on the spatial arrangement of atoms, their coordination, and the overall connectivity inside the crystal lattice. A comprehensive grasp of the crystal structure is essential in order to fully appreciate the properties and behavior of materials. This knowledge allows researchers to customize the features of materials for particular purposes, such as the development of thermoelectric devices.<sup>28</sup>

The complex details of the surface of nanosized Cu<sub>2</sub>Se, which was synthesized by solvothermal methods and sintered using spark plasma, are shown in the high-magnification scanning electron microscopy (SEM) picture seen in Figure 4(a). The presented picture provides a visual representation of

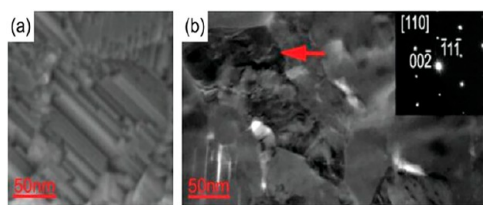


**Figure 4.** (a) High-magnification scanning electron microscope image and (b) transmission electron microscopy (TEM) image of solvothermally synthesized and spark plasma sintered nanosized Cu<sub>2</sub>Se.<sup>28</sup> Copyright *Advanced Materials* 2020, 32, 1905703.

the topographical and morphological characteristics of the material's surface at a microscopic size. The presence of nanoscale Cu<sub>2</sub>Se particles may be seen, displaying intricate surface features and distinct outlines. The scanning electron microscope (SEM) enables the examination of the fine details of particles on a surface, including their granular structure, possible aggregation, and general homogeneity. This observa-

tion facilitates comprehension of the microstructure of the material and offers vital insights for enhancing its qualities and uses.

The internal structure of the nanosized Cu<sub>2</sub>Se, which was synthesized by solvothermal methods and sintered using spark plasma, is further examined in the transmission electron microscope (TEM) picture shown in Figure 4(b). This technique offers a microscopic perspective on the elemental makeup and atomic structure of the material at the nanoscale. The transmission electron microscopy (TEM) picture allows for the observation and analysis of distinct Cu<sub>2</sub>Se nanoparticles, providing insights into their dimensions, morphologies, and crystallographic alignments. The use of transmission electron microscopy (TEM) allows for the examination of lattice fringes and defects present inside nanoparticles, hence offering valuable insights into their crystalline quality. Furthermore, it is possible to investigate potential interfaces that may exist between nanoparticles and grain boundaries. The inclusion of such intricate information facilitates the clarification of the nanoscale attributes of the material, providing significant insights for customizing its properties and comprehending its prospective uses in nanoelectronic and thermoelectric devices.<sup>28</sup> The provided figure, labeled as Figure 5(a), displays a bright-field transmission electron microscopy

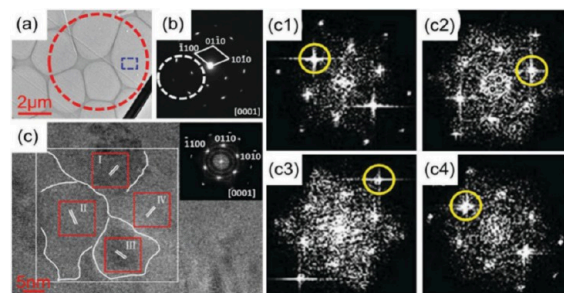


**Figure 5.** (a) Bright-field transmission electron microscopy (TEM) image of an ultrathin mosaic-structured Cu<sub>2</sub>S<sub>0.5</sub>Te<sub>0.5</sub> and (b) corresponding selected area electron diffraction pattern (SAED) of the round circled area in (a). (c) High-resolution TEM image of the blue rectangle highlighted area in (a). Inset is the fast Fourier transform (FFT) diffractogram, and (c1)–(c4) are the FFT diffractograms of selected areas in (c) marked as I, II, III, and IV. (a–c) Copyright *Advanced Materials* 2020, 32, 1905703.<sup>28</sup>

(TEM) picture that offers a comprehensive examination of a Cu<sub>2</sub>S<sub>0.5</sub>Te<sub>0.5</sub> sample with an ultrathin mosaic structure. The presented picture provides a detailed depiction of the intricate internal composition and organization of the material on a nanoscale magnitude. The presence of a mosaic-like pattern in the sample indicates the existence of diverse crystal orientations, which in turn contributes to the distinctive characteristics shown by the material. The existence of unique crystallographic orientations may be inferred by observing the borders between different mosaic domains.

The selected area electron diffraction (SAED) pattern seen in Figure 5(b) is derived from the circular region highlighted in the transmission electron microscopy (TEM) shown in Figure 5(a). Scanning electron backscatter diffraction (SAED) is a technique that offers insights into the crystallographic orientations that exist inside a given material. The diffraction pattern arises as a consequence of the interaction between electrons and the crystal lattice, giving rise to a discernible arrangement of spots. The observed dots are indicative of

distinct crystal planes and orientations, hence demonstrating the crystalline characteristics inherent in the material. The high-resolution transmission electron microscopy (TEM) picture, shown in Figure 5(c), provides a closer view of a particular location of interest, which is indicated by the blue rectangle in image (a). The presented picture offers a more detailed depiction of the atomic configuration inside the mosaic structure. The inclusion of a fast Fourier transform (FFT) diffractogram serves to enhance the characterization of the crystal lattice by converting spatial data into diffraction patterns. The FFT diffractograms labeled as Figures Scl–c4 are associated with distinct regions denoted as I, II, III, and IV within the high-resolution picture. The diffractograms provide valuable information on the specific crystallographic orientations at a local level, aiding in the identification of atom arrangements within various mosaic domains<sup>28</sup> (see the illustrations in Figure 5(a–c)).

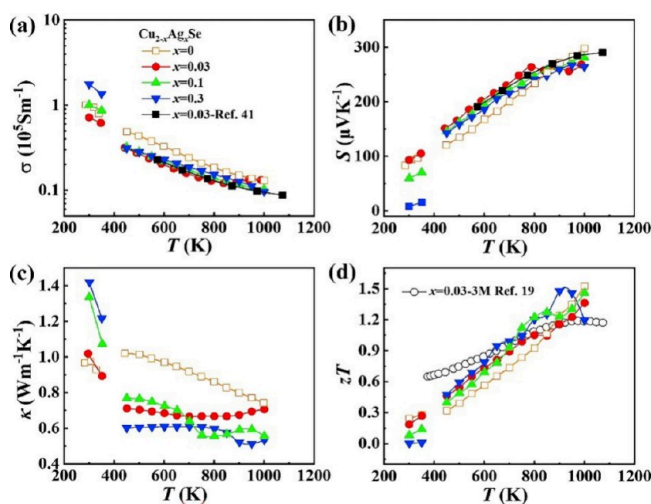


**Figure 6.** Illustration of the temperature dependencies of various properties, namely, (a) electrical conductivity ( $\sigma$ ), (b) Seebeck coefficient ( $S$ ), (c) thermal conductivity ( $\kappa$ ), and (d) dimensionless figure-of-merit ( $zT$ ), are investigated for the compound  $\text{Cu}_2-x\text{Ag}_x\text{Se}$ , where  $x$  takes on the values of 0, 0.03, 0.1, and 0.3.<sup>29</sup> Copyright *Materials Physics Today* 2021, 21, 100550.

Figure 7(a) depicts the powder X-ray diffraction patterns of  $\text{Cu}_2-x\text{Ag}_x\text{Se}$  samples at room temperature, specifically for values of  $x$  equal to 0, 0.03, 0.1, and 0.3. The diffraction patterns obtained from both pure  $\text{Cu}_2\text{Se}$  and  $\text{Cu}_1.97\text{Ag}_0.03\text{Se}$  samples exhibit a strong resemblance to the trigonal  $\text{Cu}_2\text{Se}$  phase ( $R\bar{3}m$ , ICSD-4321181), with no notable presence of extra peaks. Nevertheless, the material denoted as  $\text{Cu}_1.9\text{Ag}_0.1\text{Se}$  has distinct peaks at  $2\theta = 28^\circ$  and  $2\theta = 36^\circ$ , which become more pronounced in the case of  $\text{Cu}_1.7\text{Ag}_0.3\text{Se}$  (as seen in Figure 8).

The observed peaks in the data are consistent with the orthorhombic  $\text{CuAgSe}$  phase, as verified using elemental energy dispersive spectroscopy (EDS) mapping (Figure 9) (PDF#25-1180).

The presence of a small  $\text{CuAgSe}$  phase may be seen in  $\text{Cu}_1.97\text{Ag}_0.03\text{Se}$  (Figure 7(b)), indicating a tendency to create this secondary phase rather than incorporating it into the lattice of  $\text{Cu}_2\text{Se}$  under ambient conditions. The aforementioned behavior is consistent with the empirically observed limited solubility of silver (Ag) in copper selenide ( $\text{Cu}_2\text{Se}$ ).

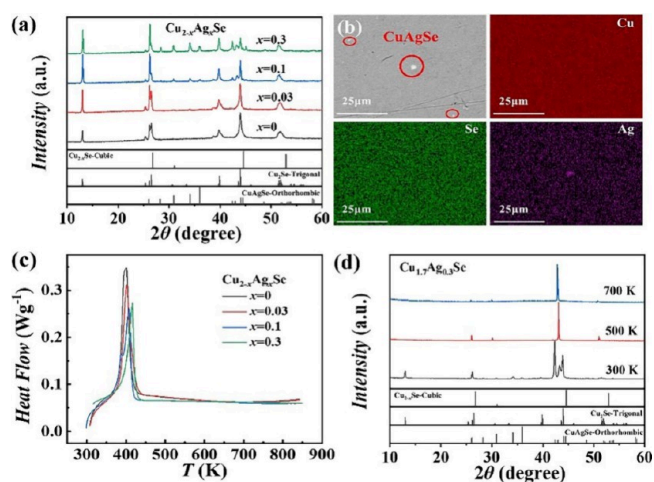


**Figure 7.** (a) Room-temperature powder X-ray diffraction (PXRD) patterns were obtained for  $\text{Cu}_2-x\text{Ag}_x\text{Se}$ , where  $x$  values of 0, 0.03, 0.1, and 0.3 were investigated. (b) A backscattered electron (BSE) imaging and element mapping were conducted on a sample of  $\text{Cu}_1.97\text{Ag}_0.03\text{Se}$ . (c) The heat flow curves for  $\text{Cu}_2-x\text{Ag}_x\text{Se}$  were measured across a temperature range of 300 to 850 K. (d) The high-temperature X-ray diffraction (XRD) patterns were obtained for bulk  $\text{Cu}_1.7\text{Ag}_0.3\text{Se}$ .<sup>29</sup> Copyright *Materials Physics Today* 2021, 21, 100550.

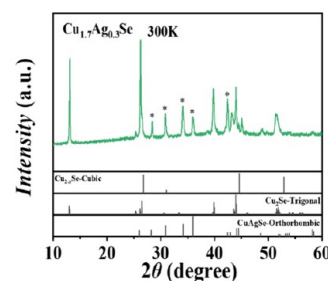


**Figure 8.** Enlarged image of the room-temperature powder X-ray diffraction (PXRD) pattern of  $\text{Cu}_1.7\text{Ag}_0.3\text{Se}$ , as seen in Figure 7(a). The diffraction peaks associated with the  $\text{CuAgSe}$  precipitates are denoted by asterisks.<sup>29</sup> Copyrights *Materials Physics Today* 2021, 21, 100550.

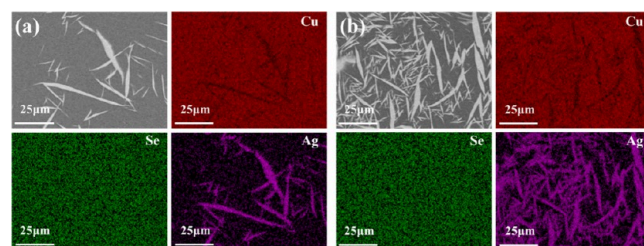


**Figure 9.** Backscattered electron (BSE) images and element mapping analysis conducted on two samples: (a)  $\text{Cu}_1.9\text{Ag}_0.1\text{Se}$  and (b)  $\text{Cu}_1.7\text{Ag}_0.3\text{Se}$ .<sup>29</sup> Copyright *Materials Physics Today* 2021, 21, 100550.

The temperature dependence of the electrical conductivity ( $\sigma$ ) for  $\text{Cu}_2-x\text{Ag}_x\text{Se}$  samples (with  $x$  values of 0, 0.03, 0.1, and 0.3) is shown in Figure 6(a). The data demonstrate the influence of the introduction of Ag on the electrical transport capabilities of the material in response to temperature variations. It is worth noting that the inclusion of even a little amount of Ag results in a substantial decrease in electrical conductivity when compared to the unmodified  $\text{Cu}_2\text{Se}$ . Moreover, this phenomenon gets more evident as the temperature increases. Figure 6(b)

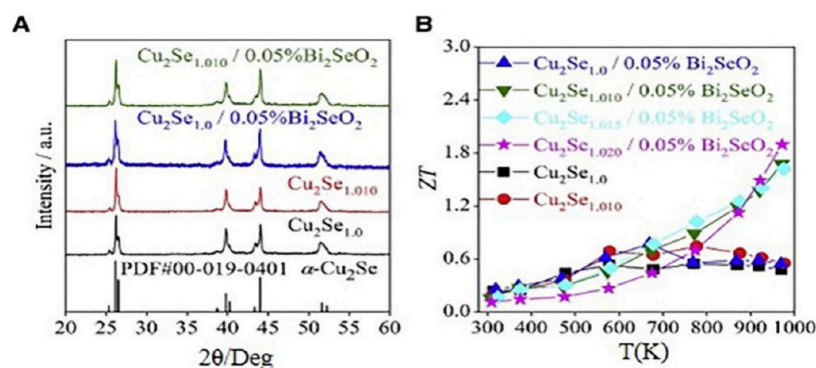
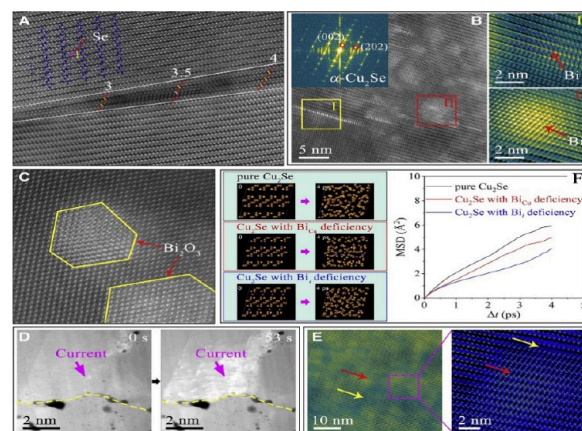


**Figure 10.** XRD patterns (denoted as A) and corresponding ZT values (denoted as B) of  $\text{Cu}_2\text{Se}_{1+x}/\text{yBi}_2\text{SeO}_2$  composites.<sup>30</sup> Copyright *Applied Thermal Engineering* 2019, 148, 238–255.

displays the temperature-dependent variation of the Seebeck coefficient ( $S$ ) for the same  $\text{Cu}_2\text{-xAg}_x\text{Se}$  samples. The shown graph illustrates the relationship between the thermoelectric voltage, which is produced in response to a temperature gradient, and the level of Ag doping. It is noteworthy that the introduction of Ag doping leads to a rise in the Seebeck coefficient, suggesting an improvement in thermoelectric efficiency, particularly under high temperature conditions. Figure 6(c) illustrates the relationship between thermal conductivity ( $\kappa$ ) and temperature. The presented graph depicts the impact of Ag doping on the thermal conductivity of the material as a function of temperature variations. It is worth mentioning that the inclusion of Ag results in a decrease in thermal conductivity within the relevant temperature range, hence enhancing the thermoelectric efficiency. In Figure 6(d), the dimensionless figure-of-merit ( $ZT$ ) is shown as a function of temperature for samples of  $\text{Cu}_2\text{-xAg}_x\text{Se}$ . The  $ZT$  value has significant importance as a key indication for evaluating the overall thermoelectric performance of a material. The presented figure demonstrates the impact of Ag doping on the  $ZT$  values within a defined temperature range, indicating a potential enhancement in the efficiency of heat-to-electricity conversion. The increased  $ZT$  values, particularly for  $\text{Cu}_{1.97}\text{Ag}_{0.03}\text{Se}$ , highlight its potential for use in thermoelectric applications within the specified temperature range.<sup>29</sup>

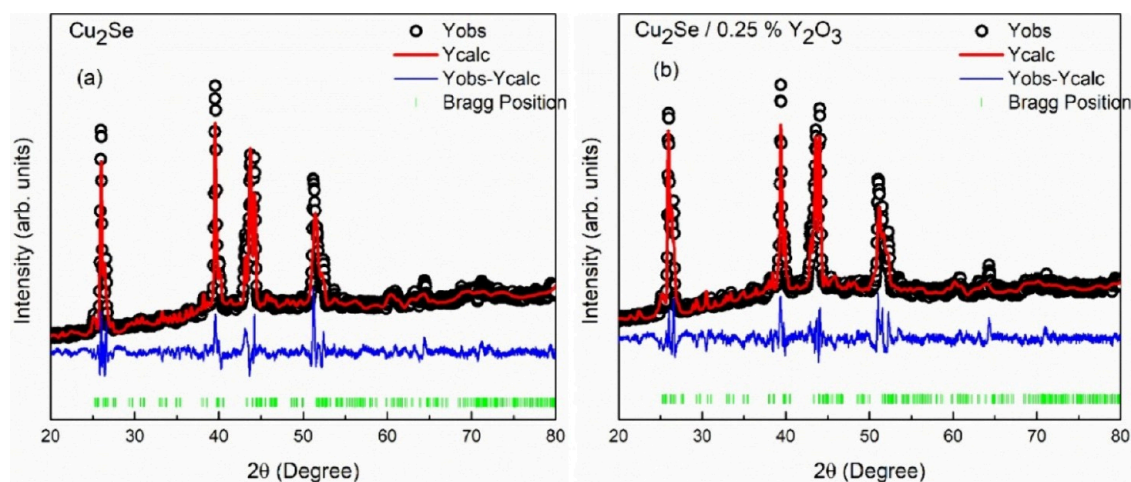
In Figure 10(A), the X-ray diffraction patterns illustrate the crystal structures of  $\text{Cu}_2\text{Se}_{1+x}/\text{yBi}_2\text{SeO}_2$  composites:  $\text{Cu}_2\text{Se}_{1.0}$ ,  $\text{Cu}_2\text{Se}_{1.010}$ ,  $\text{Cu}_2\text{Se}_{1.0}/0.05\%\text{Bi}_2\text{SeO}_2$ ,  $\text{Cu}_2\text{Se}_{1.010}/0.05\%\text{Bi}_2\text{SeO}_2$ ,  $\text{Cu}_2\text{Se}_{1.015}/0.05\%\text{Bi}_2\text{SeO}_2$ , and  $\text{Cu}_2\text{Se}_{1.020}/0.05\%\text{Bi}_2\text{SeO}_2$ . In Figure 10B, the values for thermoelectric figure-of-merit ( $ZT$ ) are shown, emphasizing the enhanced efficiency and performance achieved by changes in composition and the introduction of  $\text{Bi}_2\text{SeO}_2$  doping.<sup>30</sup>

Figure 11(A) displays the microstructure observed in bulk materials of  $\text{Cu}_2\text{Se}_{1.010}/0.05$  mol %  $\text{Bi}_2\text{SeO}_2$ . Specifically, it illustrates a dislocation characterized by a Burgers vector of  $1/6[013]$ . The movement of the dislocation will result in the release of Cu ions. The movement of the partial dislocation  $1/12[013]$  will result in the depletion of Cu ions inside the crystal. However, the occurrence of a double gliding of the dislocation will lead to the loss of both Cu cations and Se anions, facilitated by the processes of Se diffusion and evaporation. In Figure 11(B), it can be seen that Bi ions are present in two distinct regions. In area I, these ions fill the vacant spaces between the layers of atoms. On the other hand, in area II, the Bi ions replace the Cu ions at their respective



**Figure 11.** Fine microstructure in  $\text{Cu}_2\text{Se}_{1.010}/0.05$  mol %  $\text{Bi}_2\text{SeO}_2$  bulk materials: (A) Dislocation of  $1/6[013]$  causes Cu ion loss, and  $1/12[013]$  also loses Cu ions; double gliding loses Cu cations and Se anions. (B) Bi ions fill empty or replace Cu sites. (C)  $\text{Bi}_2\text{O}_3$  nanoprecipitates in grains. (D) Grain boundaries block Cu ion flux. (E) Nanodomains: Bi has the brightest contrast, hindering dislocation migration. (F) AIMD simulation: Bi hinders  $\text{Cu}^+$  ion migration.<sup>30</sup> Copyright *Applied Thermal Engineering* 2019, 148, 238–255.

positions. Figure 11(C) illustrates the presence of nanoprecipitates of  $\text{Bi}_2\text{O}_3$  among the grains. Figure 11(D) depicts an in situ transmission electron microscopy (TEM) setup where the material under investigation is subjected to both an electric current and elevated temperature. The evidence suggests that the presence of a grain boundary has the potential to impede the flow of Cu ions to some degree. Figure 11(E) illustrates the presence of nanodomains consisting of regions with a lower concentration of copper (shown by a dark contrast) intermixed with areas exhibiting a higher concentration of copper (indicated by a bright contrast). The element bismuth (Bi), which has a high atomic mass, exhibits a pronounced contrast in the high-angle annular dark-field scanning transmission electron microscopy (HAADF STEM) picture. Additionally, the presence of interstitial and doped bismuth ions hinders the migration of dislocations. Figure 11(F) depicts an ab initio molecular dynamics (AIMD) simulation whereby the Cu site is replaced by Bi and Bi is inserted between the layers. The study examines the relationship between the mean squared displacement (MSD) of  $\text{Cu}^+$  ions and the time interval  $\Delta t$ . It is shown that the presence of Bi ions in the interlayer effectively impedes the migration of  $\text{Cu}^+$  ions.<sup>30</sup>



**Figure 12.** X-ray diffraction (XRD) patterns of (a) copper selenide ( $\text{Cu}_2\text{Se}$ ) and (b) copper selenide with 0.25% yttrium oxide ( $\text{Y}_2\text{O}_3$ ).<sup>35</sup> Copyrights *Chemical Engineering Journal* 2019, 371, 593–599.

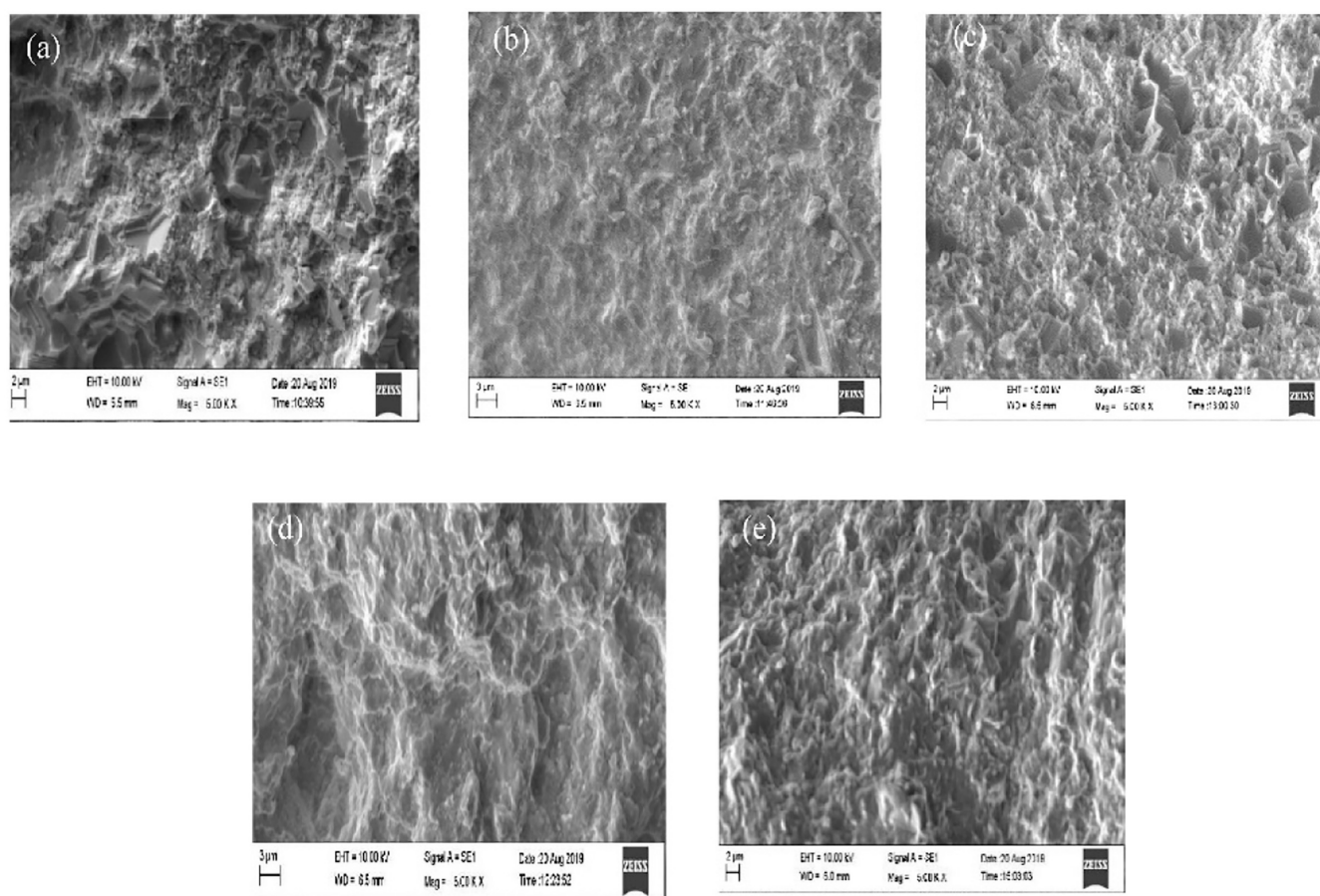


**Figure 13.** SEM micrographs of  $\text{Cu}_2\text{Se}$  with varying percentages of  $\text{Y}_2\text{O}_3$  doping: (a)  $x = 0.00$ , (b)  $x = 0.25$ , (c)  $x = 0.50$ , (d)  $x = 0.75$ , (e)  $x = 1.00$ .<sup>35</sup> Copyright *Chemical Engineering Journal* 2019, 371, 593–599.

The X-ray diffraction (XRD) examination conducted in the range of  $20^\circ$  to  $80^\circ$ , as seen in Figure 12(a) together with the Rietveld plots presented in Figure 12(b), provide confirmation of the presence of deformed monoclinic crystal structures (namely, the  $C1m1$  space group) in the manufactured composites. These findings agree with the established standard ICDD card #27–1131, with the exception of the composite with  $x = 1\%$ , which exhibits the  $P2/m$  space group. The addition of  $\text{Y}_2\text{O}_3$  does not result in the formation of secondary

phases owing to its low concentration. The investigation focused on the impact of crystallite size and strain on thermoelectric characteristics, using the Williamson–Hall (W–H) technique. The average crystallite diameters of the synthesized samples were found to be in the range of 50–230 nm. This determination was made by graphing  $\beta \cos \theta$  versus  $4 \sin \theta$ .

Figure 13(b) presents the results of the surface morphology study, which included the examination of cracked surfaces

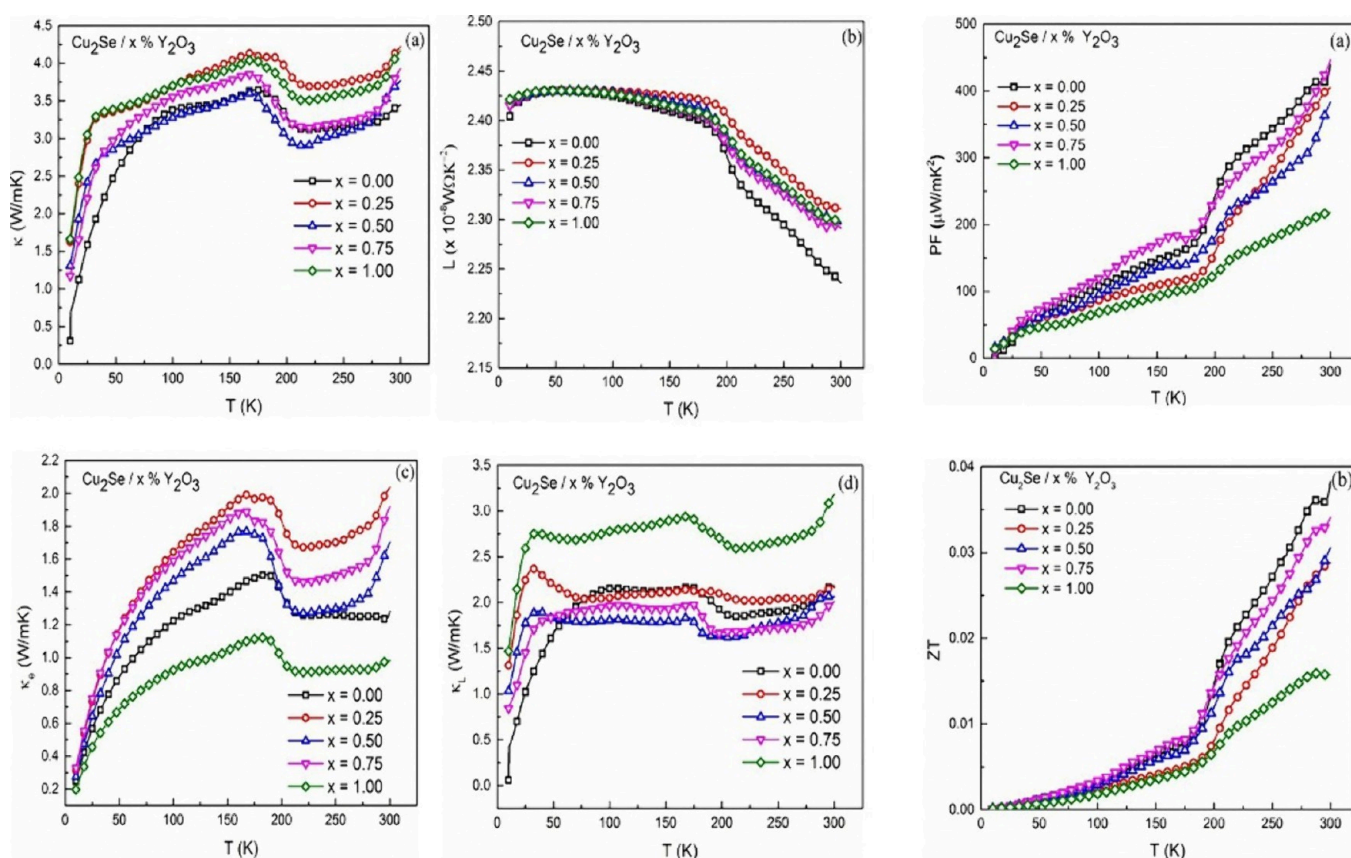


**Figure 14.** Temperature-dependent plots of  $\text{Cu}_2\text{Se}/x\% \text{Y}_2\text{O}_3$  compounds: (a) thermal conductivity, (b) Lorenz number, (c) electronic thermal conductivity, (d) lattice thermal conductivity.<sup>35</sup> Power factor and ZT are displayed on the right side. Copyright *Chemical Engineering Journal* 2019, 371, 593–599.

using scanning electron microscopy (SEM) micrographs. The SEM was operated at an electron high tension of 10 kV and a magnification of 5k $\times$ , as shown in Figure 13(a)–(e). The visual representations demonstrate the lack of pores, suggesting a significant level of density inside the sample. Nevertheless, the occurrence of uneven grain development has been reported, perhaps attributed to the process of low-temperature sintering.<sup>35</sup>

Figure 14 examines the thermal conductivity-related characteristics of  $\text{Cu}_2\text{Se}/x\% \text{Y}_2\text{O}_3$  compounds, focusing on their temperature-dependent behavior. The study of how thermal conductivity changes with temperature provides valuable information about the heat conduction characteristics, which are of great importance in thermal management applications. The temperature dependence of the Lorenz number provides insights into the behavior of charge carriers and their involvement in heat conduction. Additionally, the analysis of electronic and lattice thermal conductivity helps to clarify the respective contributions of electrons and lattice vibrations. This research contributes to a more thorough knowledge of the thermal transport properties of the materials. These findings give useful insights for possible applications and performance evaluation.<sup>35</sup>

**2.2. Heat-to-Electricity Converters Comprised of Molybdenum Disulfide (MoS<sub>2</sub>).** In a study conducted by Wang et al. in 2016, nonequilibrium molecular dynamics modeling was employed to examine the thermal characteristics of monolayer MoS<sub>2</sub> nanoribbons. The findings revealed that longer ribbons demonstrate greater thermal conductivity.

Specifically, the thermal conductivities of infinitely long zigzag and armchair MoS<sub>2</sub> nanoribbons were determined to be 54 W/mK and 33 W/mK, respectively. Additionally, it was observed that the thermal conductivity of MoS<sub>2</sub> remains relatively unaffected by uniaxial stretching, as the phonon dispersion curves remain unchanged.<sup>48</sup> In a study conducted by Zhang et al. in 2016, the theoretical analysis of hybrid nanoribbons composed of MoS<sub>2</sub> and WS<sub>2</sub> demonstrated the presence of a thermoelectric material with exceptional performance. The material exhibited a ZT of 5.5 at a temperature of 600 K, showing its significant potential for efficient utilization in applications related to the harvesting of thermal energy.<sup>49</sup> In their 2017 study, Xie et al. introduced a flexible thermoelectric nanogenerator (NG) that utilized a MoS<sub>2</sub>/graphene nanocomposite. The researchers observed that the incorporation of graphene resulted in improved electrical conductivity, leading to enhanced thermoelectric performance. This finding suggests that the nanocomposite has potential applications in harvesting thermal energy from the environment and functioning as a self-powered temperature sensor.<sup>50</sup> In their study published in 2020, Keshavarz et al. conducted a systematic evaluation of the electrochemical behaviors of thermoelectric materials based on n-type bismuth telluride in NaCl solutions. The researchers found that the nanocomposite sample, which contained MoS<sub>2</sub> nanoparticles, demonstrated enhanced passivity and decreased donor density in the passive layer when compared to the single-phase alloy with a coarse-grained structure.<sup>51</sup> In their study conducted in 2022, Jenisha et al. investigated the effects of Ni-doping in

MoS<sub>2</sub>. The results demonstrated that Ni-doping effectively enhanced the electrical conductivity while simultaneously reducing the thermal conductivity. However, the introduction of the nickel sulfide (NiS) phase resulted in a shift in the carrier type, leading to a decrease in the figure-of-merit. This finding emphasizes the existence of a trade-off between these factors when optimizing the thermoelectric performance.<sup>52</sup> In a study conducted by Tang et al. in 2022, it was observed that the piezotronic effect has the capacity to greatly recover the thermoelectric efficiency (ZT) and Seebeck coefficient of MoS<sub>2</sub> zigzag nanoribbons. The researchers found that the ZT value increased by 44 times, while the Seebeck coefficient increased by 6 times. These findings suggest an auspicious path for the development of high-performance thermoelectric devices.<sup>53</sup> In a study conducted by Yang et al. in 2023, the functionalization of MoS<sub>2</sub> nanosheets was achieved through a Lewis acid–base reaction involving AlCl<sub>3</sub> solution doping. This process led to a significant enhancement of the thermoelectric power factor by 1.8 times, along with improved mechanical flexibility. Furthermore, the researchers successfully developed a wearable thermoelectric wristband capable of generating a voltage output of 5 mV upon contact with the human body. These findings highlight the promising prospects of utilizing transition metal chalcogenides for harnessing the heat generated by the human body to power wearable electronic devices.<sup>54</sup> In a study conducted by Shalini et al. in 2023, it was observed that nanosheets of two-dimensional layered MoS<sub>2</sub> produced on carbon fabric, and with the addition of Cu exhibited improved thermoelectric properties. The nanosheets demonstrated a maximum Seebeck coefficient of approximately 13  $\mu\text{V}/\text{K}$  at a temperature of 373 K. This enhancement can be attributed to the energy-filtering effect resulting from the interfacial barrier between MoS<sub>2</sub> and Cu. Furthermore, the researchers designed a thermoelectric device utilizing these materials, which generated a voltage of 190.7  $\mu\text{V}$  when subjected to a temperature gradient of 8 K.<sup>55</sup> In a study conducted by Wang et al. in 2023, a prospective approach for enhancing the thermoelectric efficiency in devices is presented. This approach involves the manipulation of phonon thermal conductivity through the use of aperiodic superlattices, specifically those based on monolayer MoS<sub>2</sub>–MoSe<sub>2</sub>. The researchers achieved a maximum figure-of-merit of 1.38 at a temperature of 500 K.<sup>56</sup> In their study published in 2023, Jiang et al. introduced a straightforward approach to enhance the thermoelectric characteristics of materials based on single-walled carbon nanotubes (SWCNTs). They achieved this by creating independent composite films of MoS<sub>2</sub>/SWCNT that exhibit an improved Seebeck coefficient (S) and electrical conductivity ( $\sigma$ ). The researchers demonstrated the effectiveness of this method by achieving a maximum power factor of  $131.9 \pm 4.5 \mu\text{W m}^{-1} \text{K}^{-2}$  at room temperature. Furthermore, they constructed a thermoelectric device consisting of three pairs of p–n junctions, which yields a maximum output power of 0.43  $\mu\text{W}$ .<sup>57</sup> Thermoelectric performance is improved at 650 K with a power factor of  $8 \mu\text{W m}^{-1} \text{K}^{-2}$  thanks to the increased electrical conductivity and Seebeck coefficient, reduced thermal conductivity, and bipolar conduction caused by rhenium (Re) doping in MoS<sub>2</sub> through an easy hydrothermal route, according to a recent article by Arockia et al.<sup>58</sup> High flexibility, excellent power factor (548.7 nW/mK<sup>2</sup>), and ultralow internal resistance were achieved by a textile-based wearable thermoelectric generator (WTEG) using MoS<sub>2</sub> and MnO<sub>2</sub> in 2023 by Suresh et al.<sup>59</sup>, providing a potential solution

for efficient and flexible wearable thermoelectric devices. In 2023, Chaudhuri, Saumen, and their colleagues showed that the thermoelectric performance of monolayer MoS<sub>2</sub> is enhanced by subjecting it to hydrostatic pressure. As a result, there is a significant enhancement in thermopower (S) by 140% and in power factor ( $S^2\sigma/\tau$ ) by 310% and a reduction in lattice thermal conductivity ( $\kappa\text{L}$ ) by 20%. Consequently, the total measure of effectiveness (zT) is much enhanced. Monolayer MoS<sub>2</sub> has great potential as a material for both the n-type and p-type legs in thermoelectric modules.<sup>60</sup>

The atomic structure of a MoS<sub>2</sub> sheet is shown in Figure 15, showcasing two distinct kinds of vacancies. On the left side, a

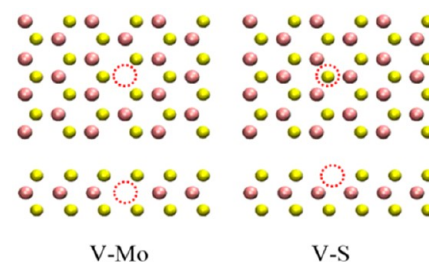


**Figure 15.** Atomic composition of a MoS<sub>2</sub> sheet, including a monovacancy consisting of molybdenum on the left and sulfur on the right.<sup>37</sup> Copyright *Materials Today Physics* 2021, 21, 100550.

vacancy involving a molybdenum (Mo) atom is seen, while on the right side, a vacancy involving a sulfur (S) atom is illustrated. The MoS<sub>2</sub> sheet exhibits a hexagonal lattice structure whereby molybdenum (Mo) and sulfur (S) atoms are organized so that each molybdenum atom is positioned between two sulfur atoms. The presence of a molybdenum vacancy on the left side of the lattice is indicative of the lack of a molybdenum atom inside the hexagonal arrangement, resulting in a vacant site. In a similar vein, the presence of a sulfur vacancy on the right side of the structure indicates the lack of a sulfur atom at that particular site. The presence of these vacancies introduces disturbances in the regular lattice arrangement, hence influencing the characteristics and behavior of the material. Consequently, the investigation and comprehension of these vacancies have significant importance in the fields of materials science and nanotechnology.<sup>37</sup>

Figure 16(a) illustrates the investigation of thermal conductivity fluctuation with ribbon length, aiming to elucidate the impact of ribbon size on heat conduction and its corresponding heat transport capacities. In addition, Figure 16(b) entails the construction of a graph where the reciprocal

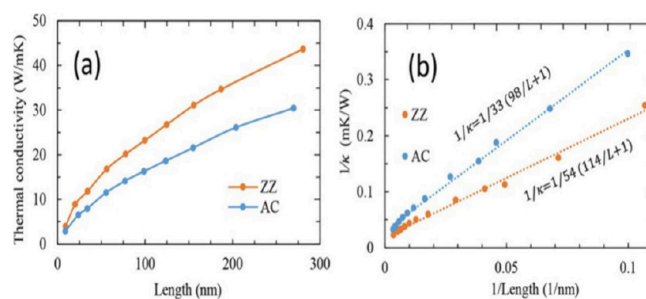


**Figure 16.** (a) Inverse of thermal conductivity as a function of length and (b) the thermal conductivity of ribbons as a function of length.<sup>37</sup> Copyright *Materials Physics Today* 2021, 21, 100550.

of thermal conductivity is plotted against the reciprocal of length. This approach offers a unique viewpoint on the behavior of heat conduction and uncovers probable underlying patterns that dictate the processes of heat transfer in these ribbons. The aforementioned investigations contribute to the advancement of our comprehension of thermal characteristics at the nanoscale, hence facilitating the development of effective materials for thermal control.<sup>37</sup>

Figure 17 displays the microstructures of p-type SP and NC samples, with Figure 17(a) representing the former and Figure

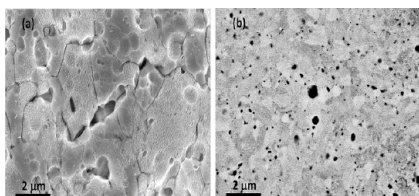


Figure 17. Microstructures of SP and NC samples, denoted as (a) and (b), respectively.<sup>39</sup> Copyright *Nature Communications* 2021, 12, 3550.

17(b) representing the latter. It is evident from the figures that the NC sample exhibits a noticeable decrease in grain size compared to the SP sample, with dimensions of 350 nm and 2.4  $\mu\text{m}$ , respectively. The inhibitory effect of MoS<sub>2</sub> nanoparticles on grain development is seen during the process of hot extrusion, therefore mitigating the expected impact of high temperatures on the migration of grain boundaries.<sup>40</sup>

Figure 18 illustrates the clear observation of MoS<sub>2</sub> nanoparticles' existence at grain boundaries, as shown by the high-resolution transmission electron microscopy (HRTEM) data presented in Figure 18(a). The electron dispersive spectroscopy (EDS) patterns provide further confirmation for the presence of the Mo and S elements (Figures 18(b–d)). It is worth noting that the high peaks of Cu seen in the patterns are attributed to the Cu grid, which serves as the sample holder. Figure 18(e) depicts the alignment of S–Mo–S layers along the (002) basal planes, exhibiting a *d*-spacing of 6.3 Å, which is in accordance with the findings reported in the existing literature. The aforementioned results together

emphasize the dispersion of MoS<sub>2</sub> inside the matrix of bismuth telluride, as shown in the transmission electron microscopy (TEM) picture at sites #2 and #3. These findings provide appreciated insights into the structural organization and composition of the materials.<sup>40</sup>

Figure 19(a,b) illustrates the X-ray diffraction (XRD) analysis, as shown in Figure 19(a), which provides confirmation of the phase structure of the synthesized materials. The observed peaks at  $2\theta = 14.10^\circ$ ,  $33.44^\circ$ ,  $39.76^\circ$ , and  $59.08^\circ$  correspond to the (0 0 2), (1 0 1), (1 0 3), and (1 1 0) planes, respectively, and align with the characteristic peaks of 2H-MoS<sub>2</sub> (JCPDS #73–1539). The absence of impurity peaks suggests the creation of a single phase. The growth dynamics of the (0 0 2) basal plane, as seen by the hydrothermal technique, exhibit an intensity ratio of 0.1% between the (0 0 2) plane and the (1 0 1) plane. The use of nickel (Ni) as a dopant induces a shift in the (0 0 2) peak and leads to the appearance of a secondary phase, especially when greater concentrations of nickel are used. The phenomenon of peak shift is seen when the Ni content is reduced, which may be attributed to the replacement of Ni<sup>2+</sup> ions on the Mo<sup>4+</sup> sites. The (1 0 3) plane is weakened by the intensified secondary phase of NiS. Increased nickel concentrations have a significant influence on the expansion of the (0 0 2) plane, resulting in the production of secondary phases that may be linked to the presence of nickel sulfide. The assessment of the solubility limit indicates that the formation of the NiS impurity phase occurs beyond a concentration of 7.5 atomic percent of nickel.<sup>41</sup>

Figure 20 displays the results of the scanning electron microscopy (SEM) examination conducted on undoped MoS<sub>2</sub> and Ni-doped MoS<sub>2</sub>, as seen in Figure 20(a0–e1). The SEM images illustrate the presence of lamellar-like layered structures in both samples. The nanosheets of pure MoS<sub>2</sub> have a disordered arrangement. An increase in the concentration of nickel leads to the transformation of well-dispersed nanosheets into a morphology resembling spheres, which is regulated by the presence of nickel (see Figure 20(c1)). The nanomaterial under investigation, denoted as NMS 7.5, has a visually organized structure consisting of nanosheets with diverse layer widths. The size of the lamellar layer exhibits an increase when the Ni concentration in undoped MoS<sub>2</sub> is increased.

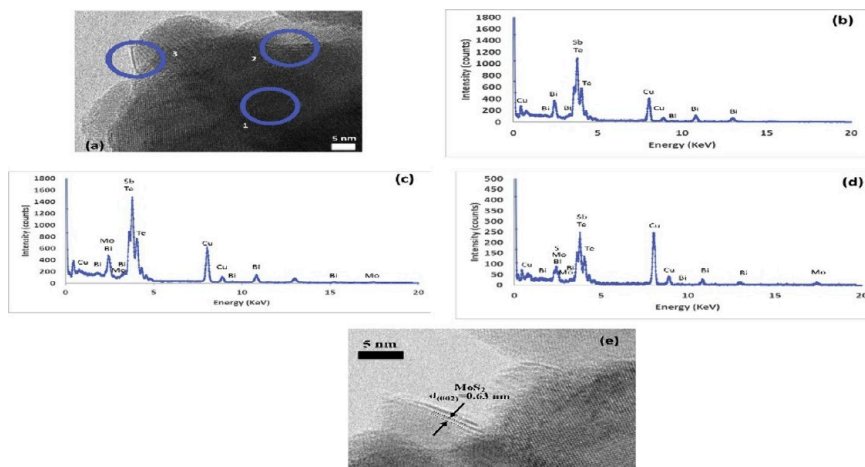
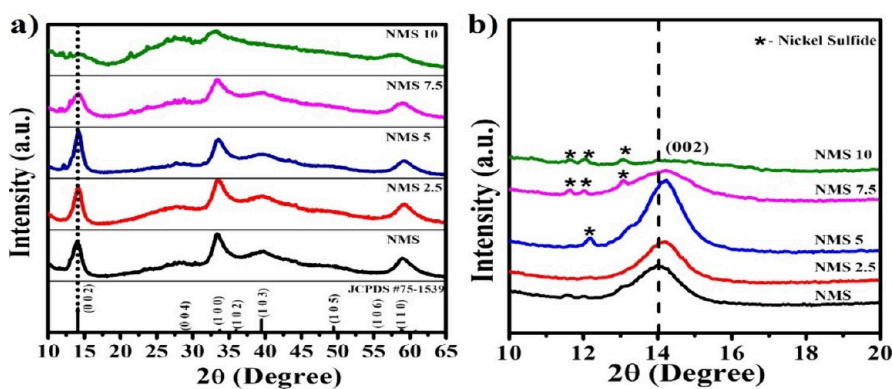
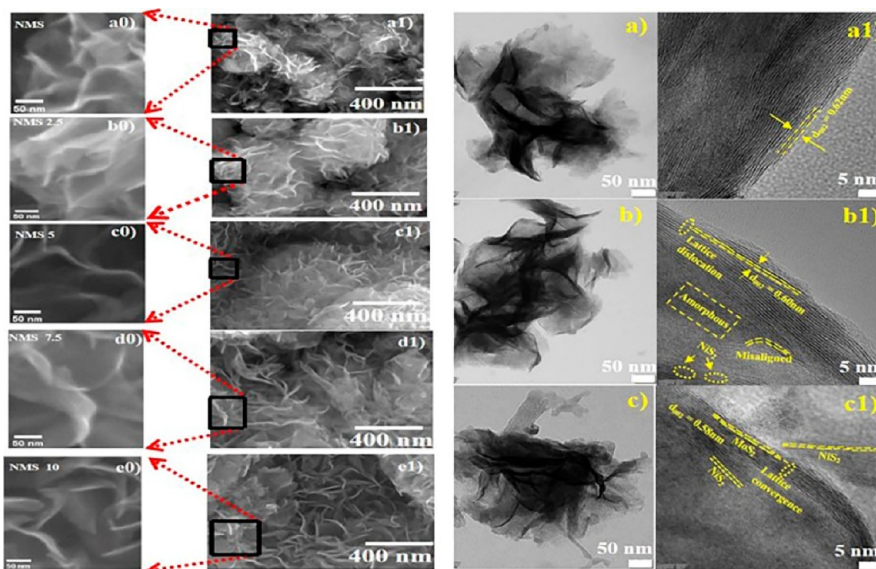


Figure 18. TEM image in panel (a) and the EDS patterns in panels (b–d) illustrate the distribution of MoS<sub>2</sub> nanoparticles in the bismuth telluride matrix at sites #2 and #3, respectively. The S–Mo–S layer is aligned with the (002) basal plane in (e) HRTEM, indicating that site #1 is a nanoparticle-free matrix.<sup>39</sup> Copyright *Nature Communications* 2021, 12, 3550.



**Figure 19.** X-ray diffraction (XRD) pattern of (a) pure molybdenum disulfide (MoS<sub>2</sub>) and (b) nickel-doped MoS<sub>2</sub> samples with varying concentrations.<sup>41</sup> Copyright *Ceramics International* 2023, 49, 9681–9690.



**Figure 20.** Scanning electron microscopy (SEM) pictures were obtained for the (a0, a1) NMS, (b0, b1) NMS 2.5, (c0, c1) NMS 5, (d0, d1) NMS 7.5, and (e0, e1) NMS 10 samples.<sup>41</sup> Copyright *Ceramics International* 2023, 49, 9681–9690.

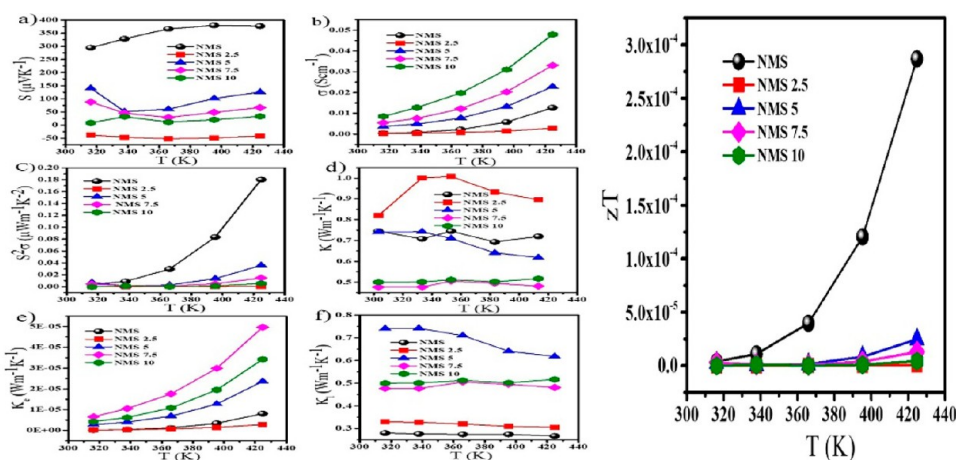


**Figure 21.** Graphs depicting the (a) Seebeck coefficient, (b) electrical conductivity, (c) and power factor changes with temperature. (d) Thermal conductivity. (e) Electronic ability to transfer heat. (f) Thermal conductivity of the lattice and ZT values.<sup>41</sup> Copyright *Ceramics International* 2023, 49, 9681–9690.

Specifically, the lamellar layer sizes for NMS 2.5, NMS 5, NMS 7.5, and NMS 10 are measured to be 9.1, 10.6, 11.5, and 12.1 nm, respectively. An indistinct boundary becomes apparent as

the concentration of nickel increases, which aligns with previous research results. The findings of NMS 10 indicate a significant augmentation in nanosheet thickness. The user's

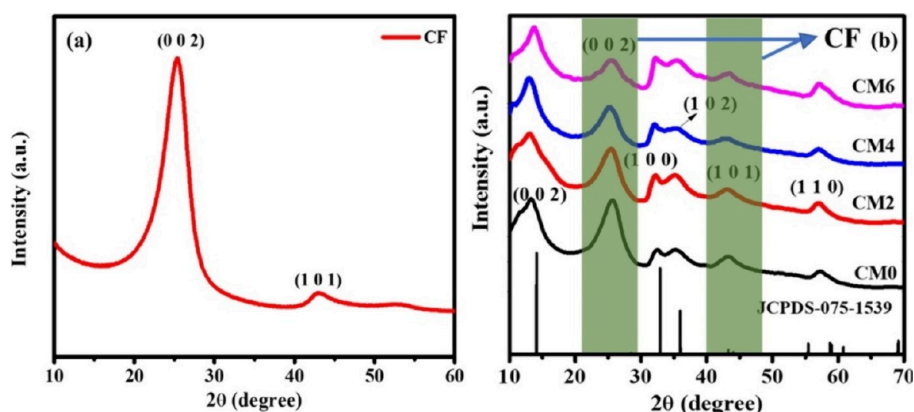


**Figure 22.** (a and b) XRD profiles of CF, MoS<sub>2</sub>, and Cu-doped MoS<sub>2</sub>.<sup>44</sup> Copyright *Energies* 2023, 16, 3010.

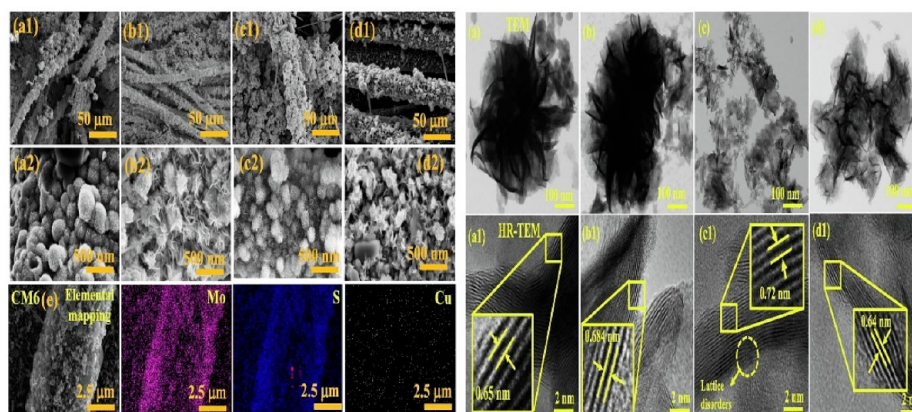


**Figure 23.** SEM images of (a1–d2) CM0, CM2, CM4, and CM6 and (e) elemental mapping of sample CM6. TEM images of CM0, CM2, CM4, and CM6 and (a1–d1) HR-TEM images of CM0, CM2, CM4, and CM6.<sup>44</sup> Copyright *Energies* 2023, 16, 3010.

text does not contain any information to rewrite. The use of high-resolution transmission electron microscopy (HRTEM) enables the acquisition of valuable information on the structural characteristics of various MoS<sub>2</sub> samples. The provided photos depict the following: (a, a1) MoS<sub>2</sub> without any doping, (b, b1) MoS<sub>2</sub> doped with 2.5 atomic percent (at %) of nickel, and (c, c1) MoS<sub>2</sub> doped with 10 at % of nickel. The provided photos provide a comprehensive examination of the atomic structure and morphological discrepancies seen in both the doped and undoped MoS<sub>2</sub> samples.<sup>41</sup>

Figure 21 illustrates the unique transition of the p-n-p Seebeck coefficient in Ni-doped MoS<sub>2</sub>, as seen in Figure 7(a). This transition has a significant impact on the behavior of charge carriers and their mobility. The undoped MoS<sub>2</sub> material has a peak value of 377  $\mu\text{V K}^{-1}$  at a temperature of 424 K. Additionally, the NMS 2.5 variant demonstrates n-type conduction. The Seebeck coefficient is reduced as the nickel (Ni) concentration is increased, mostly owing to the narrow range of Ni. The thermal band gap sequence consists of the following materials undoped with a band gap of 0.2 eV, NMS 2.5 with a band gap of 0.03 eV, NMS 5 with a band gap of 0.08 eV, NMS 7.5 with a band gap of 0.05 eV, and NMS 10 with a band gap of 0.02 eV. The trends in electrical conductivity exhibit variations, with the exception of NMS 2.5, as a result of adjustments in conduction types. Undoped molybdenum disulfide (MoS<sub>2</sub>) has a superior power factor of 1.850  $\mu\text{W m}^{-1} \text{K}^{-2}$  at a temperature of 420 K. The thermal diffusivity and conductivity of the samples doped with Ni are decreased, which may be ascribed to the influence of morphology and

interface scattering. The presence of higher amounts of nickel (Ni) is associated with an increase in electronic ( $\kappa_e$ ) and lattice ( $\kappa_l$ ) contributions, suggesting a stronger electronic impact. The NMS 7.5 exhibits improved phonon scattering, resulting in a reduction in lattice thermal conductivity attributed to lattice mismatch and shrinkage. The thermoelectric figure-of-merit (ZT) is calculated using equation  $ZT = S^2\sigma T/K$  and graphically shown in Figure 21. Throughout a temperature span of 300 to 440 K, the undoped sample has the greatest ZT value, with a maximum of 0.00028 at a temperature of 424 K. The rise in Ni concentration leads to a decrease in the thermoelectric figure-of-merit (ZT) in Ni-doped materials. This may be attributed to the formation of a secondary phase, NiS, at higher Ni concentrations. This observation highlights the significant impact of the NiS phase on the thermoelectric characteristics, hence necessitating a more comprehensive examination.<sup>41</sup>

In Figure 22(a,b), the X-ray diffraction (XRD) patterns were analyzed, indicating the presence of hexagonal MoS<sub>2</sub> on carbon fiber (CF) with a crystal structure that is well aligned. The observed peaks in the XRD patterns are consistent with the data available in the JCPDS database. Additionally, impurities and graphitic carbon were detected in both the CF and uncoated samples. Figure 23 demonstrates the examination of the surface morphology and elemental distribution through the utilization of high-resolution scanning electron microscopy (HR-SEM) and energy-dispersive X-ray spectroscopy (EDS) mapping. The results indicate that both the pristine and Cu-doped MoS<sub>2</sub> layers exhibit a consistent

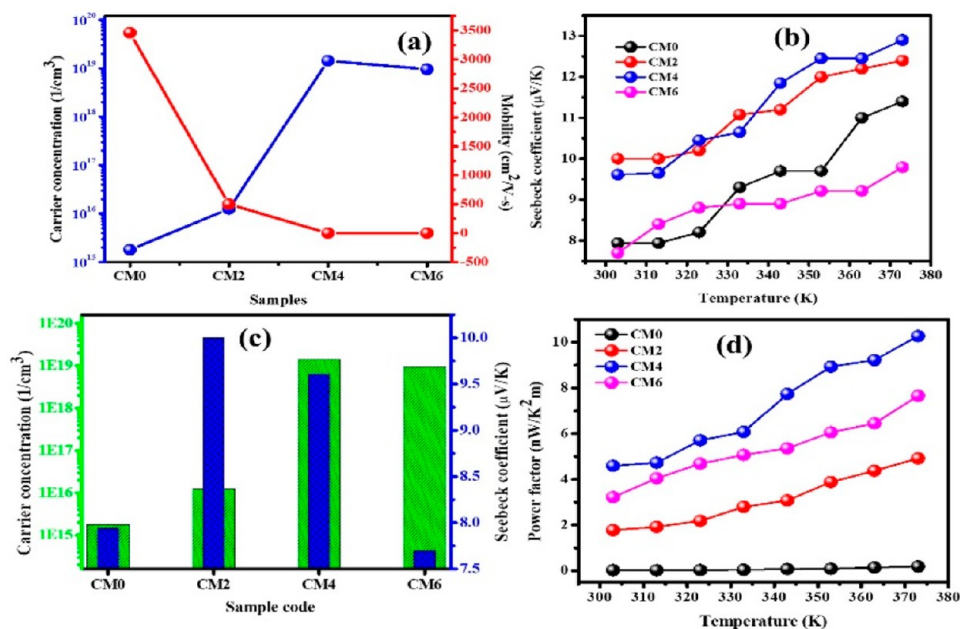


**Figure 24.** (a) Carrier concentration and mobility at room temperature, (b) temperature dependence of the Seebeck coefficient, (c) summary of carrier concentration and the Seebeck coefficient at room temperature, and (d) power factor as a function of temperature.<sup>44</sup> Copyright *Energies* 2023, 16, 3010.

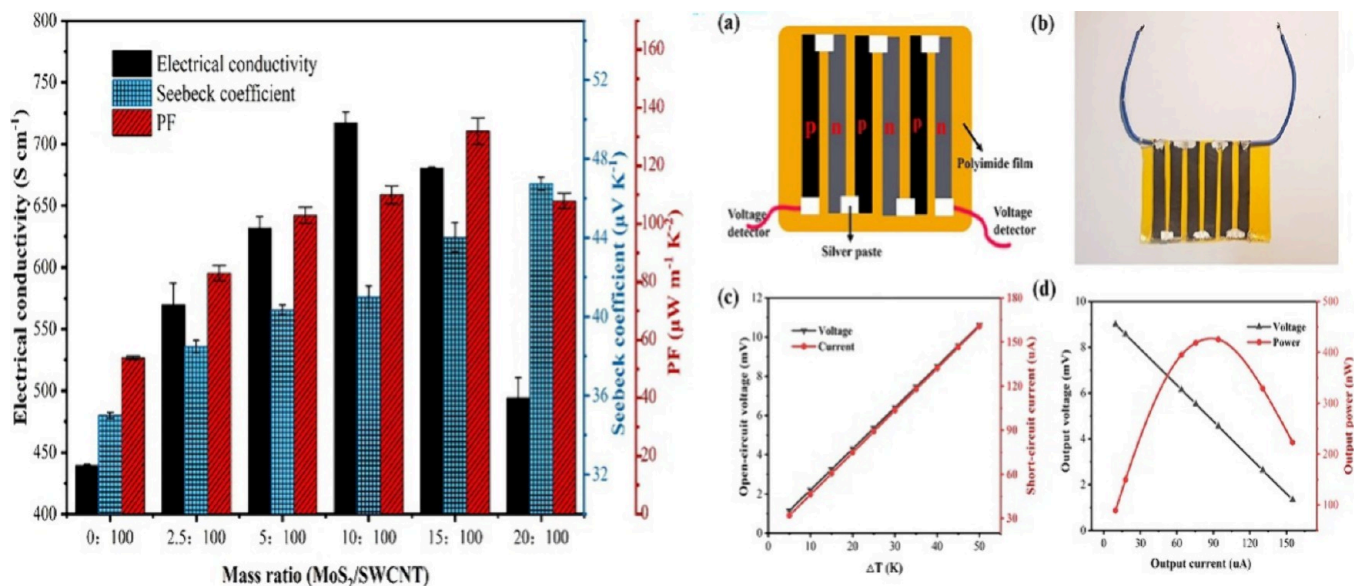


**Figure 25.** Thermoelectric characteristics of films containing varying mass ratios of MoS<sub>2</sub>/SWCNT at room temperature, along with a schematic drawing of the thermoelectric (TE) device. Additionally, the TE device is depicted in a photograph. The voltage and current generated by the equipment are shown at different temperature differences at both ends. Furthermore, the module's power/current and voltage/current curves are displayed at a temperature differential of 50 K.<sup>46</sup> Copyright *Advanced Materials* 2023, 35, 2210345.

formation of a flower-like structure composed of interconnected nanosheets on a carbon fiber (CF) substrate. This suggests that the growth of MoS<sub>2</sub> is dense and devoid of cracks and that there is a robust adhesion between the CF substrate and MoS<sub>2</sub>. Figure 23 illustrates the results of the high-resolution transmission electron microscopy (HR-TEM) examination conducted on MoS<sub>2</sub> samples that were subjected to different amounts of Cu doping. The analysis showed the presence of both agglomerated and well-dispersed nanosheets, characterized by folded edges and active sites. These findings suggest that the introduction of Cu has a significant impact on

encouraging the dispersion of nanosheets. The presence of Cu was discernible by the expansion of interlayers, the introduction of lattice disorder, and the occurrence of dislocations. Furthermore, the observed interlayer spacings were found to be in agreement with the results obtained from X-ray diffraction (XRD) analysis.

The carrier concentration and mobility at room temperature were evaluated using Hall measurements for MoS<sub>2</sub> samples with different degrees of Cu doping, as shown in Figure 24(a). The introduction of copper (Cu) into molybdenum disulfide (MoS<sub>2</sub>) resulted in an elevated carrier concentration that is

within the desirable range for thermoelectric (TE) materials. However, the carrier mobility experienced an initial decline as the concentration of Cu grew. The Seebeck coefficient, as seen in Figure 24(b), demonstrated an increase in the CM4 sample with a maximum of 4 atomic percent (at%) Cu doping, leading to enhanced thermoelectric (TE) capabilities. The observed rise in the Seebeck coefficient, namely in the comparison between CM2 and CM0 as shown in Figure 24(c), poses a challenge to the explanatory capacity of the Mott equation. Consequently, it becomes imperative to take into account the presence of interstitial and substitutional Cu atoms within the MoS<sub>2</sub> matrix. Referring to Figure 24(d), the power factor, which is influenced by the electrical conductivity and Seebeck coefficient, exhibits a significant improvement in CM4 (10.27 nW/(mK<sup>2</sup>) at 363 K) in comparison to CM0 (0.18 nW/(mK<sup>2</sup>) at 363 K). This enhancement can be attributed to the augmented synergy between the electrical conductivity and Seebeck coefficient in copper-doped molybdenum disulfide on carbon fiber samples.

Thermoelectric properties of thin films of MoS<sub>2</sub>/SWCNT with varying mass ratios are shown in Figure 25. Elevated electrical conductivity is a direct result of increasing the MoS<sub>2</sub>/SWCNT ratio. This is mainly because the contact resistance was lowered and the S- $\pi$  interaction was enhanced. Greater ratios are correlated with larger Seebeck coefficients, and positive Seebeck coefficients indicate the existence of p-type carrier transport. With 15% MoS<sub>2</sub>/SWCNT, the optimal power factor is  $131.9 \pm 4.5 \mu\text{W m}^{-1} \text{K}^{-2}$ , which is almost 2.5 times more than SWCNTs. Even after 200 bends, the composite material maintains a 94% conductivity and 90% Seebeck coefficient, demonstrating its remarkable flexibility. Three sets of p-n junctions on bendable polyimide substrates linked by silver (Ag) paste constitute a self-powering thermoelectric (TE) device, as shown in Figure 25(a) and 25(b). Using temperature variations to generate electricity is the suggested concept of this modular arrangement. At a 50 K gradient, the open-circuit voltage and current—shown in Figure 25(c)—reach 11.04 mV. The power/current and voltage/current curves are shown in Figure 25(d). At the same 50 K gradient, the ideal actual output power is  $0.43 \mu\text{W}$ . Discrepancies are ascribed to contact resistance, temperature/resistance relationships, measurement errors, and theoretical estimates, which anticipate a power of  $0.71 \mu\text{W}$ .

### 3. METHODS OF SYNTHESIS

**3.1. Thermoelectric Materials Employing Solution-Based Methodologies.** Solution-based thermoelectric materials are a category of materials that are produced and designed by solution-based techniques. These techniques involve the manipulation of chemical precursors in liquid solutions to fabricate substances with customized thermoelectric properties.<sup>61</sup> These methodologies utilize ideas derived from the fields of chemistry and materials science in order to devise and regulate the composition, structure, and morphology of materials at the nanoscale or molecular level.<sup>62</sup> Solution-based techniques refer to a variety of processes, including precipitation, sol-gel synthesis, electrode position, inkjet printing,<sup>63</sup> and others. These techniques are employed to fabricate thermoelectric materials that possess specific properties, allowing for effective conversion of temperature gradients into electrical voltage or vice versa. Consequently, these materials find applications in energy harvesting, power generation, and temperature sensing.<sup>64</sup> In their 2011

publication, Zhao et al. provide an overview of the progress, obstacles, and interdisciplinary endeavors in the synthesis of thermoelectric nanomaterials using solution-based chemistry techniques. The authors specifically emphasize the enhancement of thermoelectric performance through the customization of composition, morphology, and quantum effects. They also discuss various synthesis methods, including solvo/hydrothermal, electrochemical, and ligand-based techniques, applied to materials such as PbTe, Bi<sub>2</sub>Te<sub>3</sub>, and CoSb<sub>3</sub>.<sup>65</sup> The study conducted by Mazzi et al. in 2020 reveals the development of high-performance p-type and n-type hybrid Ag<sub>x</sub>Te/poly(3,4-ethylenedioxythiophene):polystyrene sulfonic acid (PEDOT:PSS) thermoelectric materials using an aqueous-based synthesis method. This approach resulted in remarkable power factors and substantial enhancements through the manipulation of inorganic nanostructures.<sup>66</sup> In a study conducted by Kumari et al. in 2023, the authors examined the contacting of an n-type Mg<sub>3</sub>Sb<sub>1.5</sub>Bi<sub>0.5</sub> intermetallic solid solution thermoelectric material using two different approaches: a single layer approach involving the use of Ni/Fe and a multilayer approach involving Cu or Ni in combination with a mixture of the thermoelectric material and Ni powder. The investigation revealed noticeable differences in microstructural variations and interfacial characteristics between the two approaches. However, the electrical contact resistance values achieved were found to be comparable. These findings provide valuable insights into effective strategies for achieving improved performance in thermoelectric devices through appropriate contacting techniques.<sup>67</sup>

Figure 26 shows how renewable energy is converted into electricity. Piezoelectric or turbine systems may capture

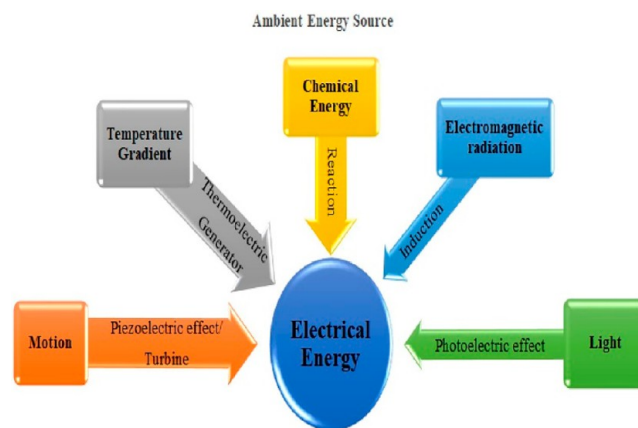


**Figure 26.** Schematic diagram of thermoelectric materials employing solution-based methodologies.<sup>68</sup> Copyright *Electricity* 2021, 2, 359–386.

mechanical oscillation, sea waves, hydroelectric power, and wind. Thermoelectric generators use light, chemical energy (from reactions, induction, and photoelectric effects), and temperature gradients. Statistics show that 25% of electricity production comes from renewable sources, and 85% by 2050. The picture also highlights energy recovery solutions including flue gas heat recovery, flywheel energy storage, and hybrid pneumatic power systems that can recover kinetic or thermal energy. Their ability to recuperate squandered energy makes these systems strong.

**3.2. Thermoelectric Material Production by Hydrothermal Means.** The hydrothermal synthesis method was

employed to produce PbTe nanowires that possess a uniform single-crystalline structure and a distinctive pearl-necklace shape. These nanowires have diameters smaller than the excitonic Bohr radius. The resulting nanowires exhibit enhanced thermoelectric performance, particularly in terms of the Seebeck coefficient. At room temperature, the Seebeck coefficient reaches approximately  $307 \mu\text{V}/\text{K}$ , surpassing the performance of bulk PbTe by up to 16%.<sup>69</sup> The hydrothermal synthesis of nanostructured p-type  $\text{Bi}_0.4\text{Sb}_{1.6}\text{Te}_3$  material has demonstrated significant thermoelectric potential. At a temperature of 398 K, the material exhibits a peak ZT value of 1.26. This enhancement in thermoelectric performance is attributed to the unique nanostructures within the material, which effectively scatter phonons and thereby reduce thermal conductivity. These findings suggest that the material is well-suited for applications in thermoelectric energy conversion.<sup>70</sup> PbTe nano cubes are synthesized using a hydrothermal method that does not involve the use of organic solvents or surfactants. The resulting nano cubes have sizes ranging from 80 to 100 nm. Additionally, bulk PbTe with a nanostructured morphology is obtained through hot-pressing. This nanostructured bulk material exhibits a significant Seebeck coefficient and reduced electrical conductivity, attributed to energy filtering effects. Moreover, the thermal conductivity is lowered due to effective scattering of phonons at grain boundaries. These combined factors contribute to the impressive thermoelectric performance of the material, with a peak ZT value of 0.78 achieved at a temperature of 450 K.<sup>71</sup> In this study, a hydrothermal method was utilized to successfully produce  $\text{Sb}_2\text{Te}_3$ –Te barbell-like heterogeneous nanostructures. The synthesis process involved careful control of reaction conditions. The resulting nanostructures displayed encouraging thermoelectric properties, such as an electrical conductivity of  $150.2 \text{ S cm}^{-1}$  at room temperature and a Seebeck coefficient of  $148.1 \mu\text{V K}^{-1}$ . Moreover, at a temperature of 550 K, the nanostructures exhibited a maximum power factor of  $1.02 \text{ mW K}^{-2} \text{ m}^{-1}$ , indicating their potential for use in thermoelectric applications.<sup>72</sup> The synthesis of  $\text{Bi}_0.5\text{Sb}_{1.5}\text{Te}_3$  compounds with irregular hexagonal sheet morphology was achieved through hydrothermal synthesis at a temperature of  $150 \text{ }^\circ\text{C}$  for a duration of 24 h. The resulting compounds were characterized using X-ray diffraction (XRD) and field emission scanning electron microscopy (FESEM). The analysis shows that the nanosheets exhibited a parallel stacking arrangement, forming sheet-agglomerates, which can be attributed to the presence of temperature gradients during the synthesis process. These findings indicate the potential of these compounds for use in thermoelectric applications, as reported in a previous study.<sup>73</sup> The synthesis of PbS–PbTe core–shell heterostructured nanorods with adjustable phase ratios is achieved using a direct hydrothermal method. The resulting nanorods are thoroughly characterized using multiple techniques. Thermoelectric transport measurements demonstrate an improved power factor, with a peak value of  $294 \mu\text{W (m K}^2)^{-1}$  observed at room temperature for the sample prepared with a molar ratio of 20 between PbS and Te precursors.<sup>74</sup> The thermoelectric properties of a composite material consisting of micro/nano  $\text{Cu}_2\text{-xS}$  particles have been significantly improved using a hydrothermal synthesis method. This composite material demonstrates an impressive power factor of  $10.1 \mu\text{W cm}^{-1} \text{ K}^{-2}$  and a high ZT max value of 1.1 at a temperature of 773 K. These results are particularly noteworthy as they address the

inherent challenges associated with the interrelationship between electrical and thermal conductivity in copper sulfides, thus making this composite material highly suitable for thermoelectric applications.<sup>75</sup> The researchers propose a novel method for synthesizing nanostructured SnSe integrated with Se quantum dots, utilizing an in situ magnetic field-assisted hydrothermal synthesis. This method yields a remarkable ZT of approximately 2.0 at a temperature of 873 K. The improved ZT is achieved through enhancements in the power factor and reductions in thermal conductivity. These findings suggest that this approach holds promise for the design of future thermoelectric materials.<sup>76</sup> The hydrothermal synthesis of  $\text{Bi}_2\text{Te}_3$  nanostructures with different morphologies (nanoparticles, nanoplates, nanoflowers, and nanotubes) is easily achieved by controlling the pH. This phenomenon has been extensively studied using various characterization techniques. The results indicate that the growth mechanism involves the formation of primary nanoplates and hierarchical structures. These nanostructures show promise as thermoelectric materials due to their reduced thermal conductivity and the modification of their potential energy band structure.<sup>77</sup> In this study, a novel methodology is utilized to fabricate  $\text{Bi}_2\text{S}_3 + x \text{ mL}$  reduced graphene oxide (rGO) nanocomposites through hydrothermal synthesis and tubular sintering. The objective is to reduce thermal conductivity and enhance the thermoelectric figure-of-merit. Notably, the  $\text{Bi}_2\text{S}_3/\text{rGO}$  (10 mL) nanocomposite exhibits a ZT value of 0.22 at 577 K, indicating promising prospects for optimizing the thermoelectric properties of  $\text{Bi}_2\text{S}_3$ .<sup>78</sup>

Figure 27 depicts the schematic representation of hydrothermal therapy. In the first phase of the hydrothermal process,

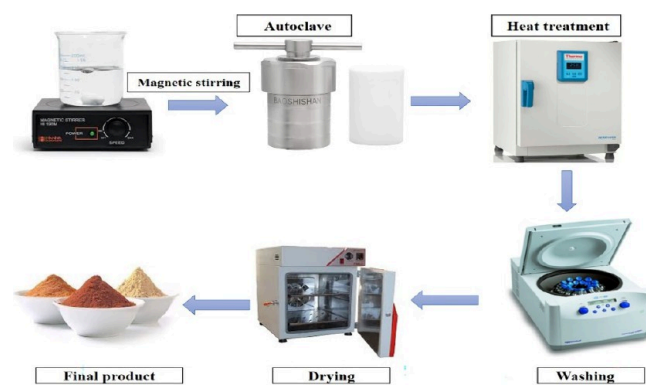


Figure 27. Schematic diagram of hydrothermal method. Created by the authors of this paper.

materials are subjected to magnetic stirring in order to attain a homogeneous mixture. Afterward, the resulting mixture is transferred into a Teflon-lined autoclave. Subsequently, the Teflon-lined autoclave is placed in an oven for a pre-established heat treatment, during which the heating parameters are fine-tuned to correspond with the properties of the materials used. Following the heat treatment process, the materials are then cooled and subjected to a washing procedure using deionized water or other chemical agents such as ethanol to guarantee thorough cleaning. Following the cleaning process, the samples are carefully moved to an oven for thorough drying, thereby removing any residual moisture. The ultimate outcome is obtained after it has fully dried. The final product undergoes a comprehensive characterization

process, which involves X-ray diffraction (XRD), scanning electron microscopy (SEM), and transmission electron microscopy (TEM). Furthermore, the performance assessment encompasses the examination of crucial aspects such as electrical conductivity, thermal conductivity, power factor, and overall functionality. These systematic inspections facilitate the acquisition of a thorough understanding of the structural, morphological, and functional features of the material.

**3.3. Alloys Composed of Solid Reactions and Nanoparticles.** This study investigates the improvement of thermoelectric efficiency in nanoscale SnTe by including MgAgSb alloy nanoparticles and indium through codoping. This codoping strategy leads to enhanced electrical and thermal properties, ultimately culminating in a high ZT value of 1.41 at a temperature of 835 K.<sup>79</sup> The optimization of thermoelectric properties in SnTe is achieved through the introduction of MgAgSb alloy nanoparticles as codopants at low concentrations. This codoping strategy enhances the Seebeck coefficient by promoting valence band convergence and generating resonant states. Additionally, it improves carrier mobility by reducing the presence of Sn vacancies, leading to a high-power factor. Furthermore, the thermal conductivity is significantly reduced. As a result, a remarkable ZT value of 1.41 is achieved at a temperature of 835 K.<sup>80</sup> The thermoelectric properties of  $\text{Ca}_3\text{Co}_4\text{O}_{9+\delta}$  were greatly improved by employing a dual optimization approach that involved elemental substitutions and dispersion of SiC nanoparticles in double-layered oxide samples  $\text{Ca}(\text{Ba}, \text{Sr})_3\text{Co}_4\text{O}_{9+\delta}$ . This resulted in an optimal dimensionless thermoelectric ZT value of 0.25 at 923 K for both  $\text{Ca}_{2.93}\text{Sr}_{0.07}\text{Co}_4\text{O}_{9+\delta} + 0.1 \text{ wt } \% \text{ SiC}$  and  $\text{Ca}_{2.9}\text{Ba}_{0.1}\text{Co}_4\text{O}_{9+\delta} + 0.1 \text{ wt } \% \text{ SiC}$ .<sup>81</sup> This research paper provides a thorough examination of bulk nanostructured  $\text{Mg}_2\text{Si}_{0.4}\text{Sn}_{0.6}$  thermoelectric materials. The materials were synthesized using mechanical alloying and spark plasma sintering techniques. The study investigates the microstructure, transport properties, and aging effects of these materials. Additionally, a model is developed to accurately quantify the influence of nano/microstructural parameters on lattice thermal conductivity, which is essential for improving the performance of thermoelectric materials.<sup>82</sup> This study demonstrates the successful improvement of the power factor and decrease in lattice thermal conductivity in  $\text{TiZr}_x\text{NiSn}$  Half-Heusler alloys through additional Zr doping. As a result, a significantly improved peak ZT value of 0.88 at 773 K and an average ZT value of 0.62 within the temperature range of 373–773 K are achieved. These results deliver valuable insights into the optimization of thermoelectric performance through the modulation of microstructure.<sup>83</sup> The main aim of this review is to evaluate the present condition of composite thermoelectric materials that incorporate embedded nanoparticles. It explores the various mechanisms employed to improve the thermoelectric properties of these materials, as well as the experimental techniques used for their preparation. Additionally, it emphasizes the necessity for systematic investigations that establish a correlation between the effects of nano-inclusions and the measured properties of the materials. This correlation is crucial for the further advancement of this particular field.<sup>84</sup> The structural and thermoelectric properties of ZnAlS nanoparticles were manipulated by adjusting the concentration of Al atoms (ranging from 1% to 4%) through a solid-state reaction. This modulation resulted in an observed enhancement of the Seebeck coefficient and electrical

conductivity at a 4% Al concentration. This improvement can be attributed to the formation of potential secondary phases within the ZnS lattice, as reported in a previous study.<sup>85</sup> Composite thermoelectric materials  $(\text{CuO})(\text{ZnO})_{1-x}$ , which are based on ZnO and CuO, were synthesized using a solid-state reaction. The synthesis process led to variations in the structure, morphology, and electrical properties of the materials as the CuO content increased. Notably, a sample with a CuO content of 0.75 ( $\text{CuO}_{0.75}\text{ZnO}_{0.25}$ ) exhibited a higher power factor of  $12.92 \mu\text{W}/\text{mK}^2$  at a temperature of approximately 575 K.<sup>86</sup> This study introduces a novel method that utilizes electrodeposition to apply inorganic thermoelectric layers onto the surfaces of single-walled carbon nanotubes (SWCNTs). The results demonstrate that this approach leads to enhanced thermoelectric performance, as evidenced by the improved power factor of Sb<sub>2</sub>Te<sub>3</sub>-coated SWCNT films. These findings provide valuable insights for the development of flexible thermoelectric materials with high performance capabilities.<sup>87</sup>

The schematic in Figure 28 illustrates the blending of a solution including finely dispersed raw material and carrier,

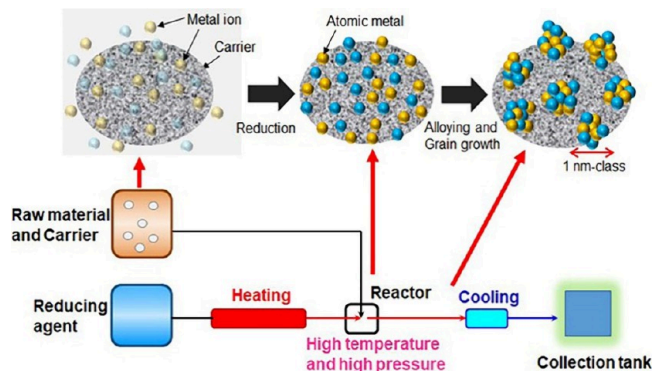


**Figure 28.** Schematic diagram of solid reaction and nanoparticle alloys. Copyright [https://www.jst.go.jp/pr/announce/20190930/index\\_e.html](https://www.jst.go.jp/pr/announce/20190930/index_e.html).

coupled with a heated reducing agent, inside a reactor working under high temperature and pressure conditions. In this setting, metal ions are reduced to produce metal atoms on the carrier material. Following that, the metal atoms experience concurrent enlargement and alloying on the carrier. In order to inhibit particle aggregation, the combined solution is quickly chilled. The careful cooling procedure leads to the creation of a catalyst that contains solid-solution alloy nanoparticles in the subnanometer size range, which are supported on the carrier material.

**3.4. Crystallization and Processes Requiring High Temperatures.** The introduction of Tb ions into polycrystalline  $\text{Ca}_3\text{Co}_4\text{O}_9$  by researchers has resulted in a remarkable improvement in thermoelectric response. This achievement has led to the attainment of a record-breaking ZT value of 0.74 at a temperature of 800 K. This significant progress contributes to the ongoing efforts in developing materials for efficient and eco-friendly conversion of waste heat energy.<sup>88</sup>  $\text{Na}_x\text{CoO}_2\text{-}\delta$  single crystals demonstrate significant potential as thermoelectric materials as temperature increases, as evidenced by a power factor of  $7.7 \text{ mW m}^{-1} \text{ K}^{-2}$  and a figure-of-merit (ZT) of 1.5 at 800 K. These values are above the threshold for efficient high-temperature thermoelectric materials, as indicated by previous research.<sup>89</sup> This perspective offers a comprehensive

examination of the evolutionary path and contemporary advancements in the field of thermoelectric nanocomposites. It draws inspiration from the groundbreaking work of Mildred S. Dresselhaus in the 1990s, shedding light on significant milestones and emerging directions in the domain of thermoelectric energy conversion.<sup>90</sup> The Yb<sub>14</sub>MnSb<sub>11</sub> compound, which belongs to the Zintl family, represents a significant advancement in the field of high-temperature p-type thermoelectric materials. It exhibits a notable improvement in efficiency and figure-of-merit when compared to SiGe. This breakthrough marks a new era in thermoelectric power generation and holds great promise for the development of segmented devices.<sup>91</sup> The unique chain structure of single-crystal Ca<sub>3</sub>Co<sub>2</sub>O<sub>6</sub> is associated with its promising thermoelectric properties at high temperatures. These properties include a positive Seebeck coefficient, low thermal conductivity, and a ZT value of approximately 0.15 at 1073 K. These characteristics highlight the material's potential as a chemically stable and efficient thermoelectric material for applications requiring high temperatures.<sup>92</sup> The precise numerical value of the dimensionless figure-of-merit (zT) for SrAl<sub>2</sub>Si<sub>2</sub> is not supplied within the offered material. The passage solely indicates that the compound's low zT value is affected by a greater contribution of lattice thermal conductivity, as stated.<sup>93</sup> The precise numerical values of the dimensionless figure-of-merit (zT) for the CaMn<sub>1-x</sub>Nb<sub>x</sub>O<sub>3 ± δ</sub> compounds, which exhibit various electron-doped manganate phases ( $x = 0.02, 0.05, \text{ and } 0.08$ ), are not included in the provided information. The paragraph discusses the promise of thermoelectric materials exhibiting high power factors and low thermal conductivity, as shown by ZT values exceeding 0.3.<sup>94</sup> This review article aims to provide a thorough examination of the latest developments in high-temperature thermoelectric materials, with a specific emphasis on semiconducting large bandgap oxides. This study examines the impact of crystallographic defects, superstructures, and different doping techniques on the thermoelectric performance. It provides valuable insights into the optimization of power factors and the reduction of lattice thermal conductivity, hence enhancing the suitability of these materials for high-temperature applications.<sup>95</sup> The objective of this research is to examine the changes in the structure of MgAgSb within a temperature range of 27–420 °C. The findings of this study demonstrate the existence of three different crystal structures and highlight the significance of stabilizing the phase that exhibits favorable thermoelectric performance at normal temperature.<sup>96</sup> The present investigation effectively achieved the synthesis of single-phase CaMnO<sub>3</sub> by employing acetate starting materials. The resulting material was subjected to structural and thermoelectric property investigations, which provided valuable insights into its potential as a thermoelectric material for enhancing energy usage efficiency.<sup>97</sup> In this study, a SnTe precursor that does not contain thiols is employed to produce nanoscale SnTe crystals and engineer SnTe-Cu<sub>2</sub>SnTe<sub>3</sub> nanocomposites. This approach leads to enhanced electrical conductivity and reduced lattice thermal conductivity, resulting in significantly improved thermoelectric performance. The achieved power factors reach up to 3.63 mW m<sup>-1</sup> K<sup>-2</sup> and figures-of-merit reach up to 1.04 at 823 K. These findings represent a significant advancement over the performance of pure SnTe and have potential implications for medium- to high-temperature applications.<sup>98</sup>

Figure 29 depicts the time–temperature–transformation (TTT) diagram which illustrates the relationship between

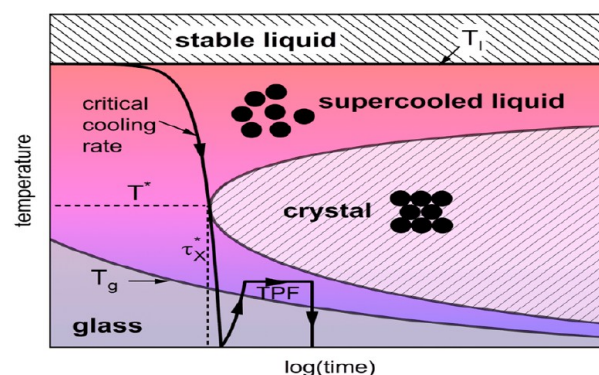


**Figure 29.** Schematic diagram of high-temperature reaction and crystallization.<sup>99</sup> Copyright Gross, Oliver. *Precious metal based bulk glass-forming liquids: Development, thermodynamics, kinetics and structure*; 2018.

time, temperature, and structural phases in a metallic liquid with the capacity to undergo glass formation. The critical cooling rate ( $R_c$ ) prevents crystallization from occurring below the liquidus temperature ( $T_l$ ), hence preserving the glass transition structure at  $T_g$ . The minimum time needed for crystal formation ( $\tau^*$ ), which occurs at temperature  $T^*$ , is the primary hindrance to the process of crystallization. Thermoplastic forming (TPF) is a process that involves heating a glassy sample, manipulating it while it is in a supercooled liquid state, and then cooling it below the glass transition temperature ( $T_g$ ) to prevent crystallization. The TTT diagram offers guidance for establishing the necessary processing parameters to achieve the specified material properties.

**3.5. Thermoelectric Materials Doped with p-Type Impurities.** In this study, a straightforward approach is utilized to synthesize high purity MnTe by integrating mechanical alloying (MA) and spark plasma sintering (SPS) techniques. The incorporation of sodium doping is found to be an effective means of adjusting the carrier concentration, leading to remarkable thermoelectric properties (Table 1). Specifically, the resulting MnTe material exhibits a high-power factor exceeding 900  $\mu\text{W m}^{-1} \text{K}^{-2}$  and achieves a peak ZT value surpassing 1.0 at 873 K. These findings highlight the potential of MnTe as a promising thermoelectric material suitable for medium-temperature applications.<sup>100</sup> The heavy-band half-Heusler alloys, specifically the p-type FeNbSb alloys, when doped with a significant amount of Hf, demonstrate an impressive figure-of-merit (zT) of around 1.5 at a temperature of 1200 K. This enhanced zT value is attributed to the optimized electrical power factor and reduced thermal conductivity of the material. Consequently, these alloys show promise for efficient and high-temperature thermoelectric power generation, with practical performance in thermoelectric modules.<sup>101</sup> By utilizing in situ synthesis techniques to form Ag<sub>3</sub>Sb nanostructures within p-type Ag-doped ZnSb, a noteworthy thermoelectric figure-of-merit (ZT) of 1.15 is attained at a temperature of 670 K. This achievement can be attributed to the optimization of carrier concentration, reduction in lattice thermal conductivity, and exceptional thermal stability. These findings underscore the potential of ZnSb as a promising thermoelectric material that is both efficient and stable, while also being cost-effective. Con-

Table 1. Thermoelectric Material Comparative Analysis of Key Characteristics and Performance

Material	Synthesis/Methods	Thermoelectric Performance	Key Features/Contributing Factors	Ref.
Cu <sub>1.982</sub> Bi <sub>0.006</sub> Se	Incorporation of bismuth	ZT = 0.43 at 373 K	Decreased number of charge carriers, enhanced power factor, reduced thermal conductivity of the carrier	35
Cu <sub>1.97</sub> Ag <sub>0.03</sub> Se	Annealing and melting at high temperatures	Improved thermoelectric characteristics, sustained stability	Introducing Ag, a rational approach to leg geometry	37
AgCuTe/Cu <sub>2</sub> Se multilayered nanostructures	Incorporation of Cu <sub>2</sub> Se into AgCuTe	ZT ≈ 1.13 (average between 523 and 723 K)	Decrease in heat conduction, creation of nanostructures with several layers	40
Cu <sub>2</sub> Se with Sb substitution	Analysis conducted using density-functional theory (DFT)	ZT = 0.47 at 523 K	Substituting Sb on Se sites leads to a significant improvement in performance	42
Hybrid nanoribbons (MoS <sub>2</sub> and WS <sub>2</sub> )	Theoretical analysis	ZT = 5.5 at 600 K	Hybrid nanoribbons have outstanding thermoelectric performance	49
Electrochemical characteristics of bismuth telluride with n-type conductivity	Mechanical alloying	Increased passivity, decreased donor density in the passive layer	Assessment of the electrochemical properties and the function of the nanocomposite sample	51
Ni-doping in MoS <sub>2</sub>	Hydrothermal method	Increased electrical conductivity, decreased thermal conductivity	Impact of Ni-doping and the trade-off between several elements	52
Nanosheets of MoS <sub>2</sub> doped with Cu on a carbon fabric	Hydrothermal method	Enhanced thermoelectric characteristics	Copper-doped layered nanosheets exhibiting an energy-filtering function	55
Manipulation of phonon thermal conductivity	Aperiodic superlattices (MoS <sub>2</sub> -MoSe <sub>2</sub> )	ZT = 1.38 at 500 K	Manipulation of phonon thermal conductivity, aperiodic superlattices	56
MoS <sub>2</sub> /SWCNT composite films	MoS <sub>2</sub> /SWCNT composite films that are independent	Power factor of 131.9 ± 4.5 μW m <sup>-1</sup> K <sup>-2</sup> at room temperature	Improvement of the Seebeck coefficient and electrical conductivity for the purpose of creating a thermoelectric device	57
PbTe nanowires	Hydrothermal synthesis	Thermoelectric performance has been improved, reaching a peak ZT value of 1.26.	Structure of the material is uniform and consists of a single crystal. It has a shape like a pearl necklace.	69
Bi <sub>0.4</sub> Sb <sub>1.6</sub> Te <sub>3</sub> nanostructured material	Hydrothermal synthesis	Peak ZT = 0.78 at 450 K	Shape of nanostructures enables efficient scattering of phonons	70
PbTe nanocubes	Organic solvent-free hydrothermal technique	Peak ZT = 0.78 at 450 K	Nanomaterial with an organized composition, efficient disruption of phonons at the interfaces between grains	71
Heterogeneous nanostructures with a barbell-like shape consisting of Sb <sub>2</sub> Te <sub>3</sub> and Te	Hydrothermal synthesis	Power factor of 1.02 mW K <sup>-2</sup> m <sup>-1</sup> at 550 K	Nanostructures resembling barbells, arranged in a parallel stacking formation	72
Nanorods with a core-shell structure consisting of PbS and PbTe	Hydrothermal method	Enhanced power factor, maximum ZT = 1.1 at a temperature of 773 K	Modifiable phase ratios, efficient resolution of difficulties in copper sulfides	75
Integration of SnSe with Se quantum dots	Process of synthesizing materials using a hydrothermal method, with the assistance of a magnetic field applied at the same location	Peak ZT ≈ 2.0 at 873 K	Improvement in figure-of-merit, decrease in thermal conductivity	76
Bi <sub>2</sub> S <sub>3</sub> /rGO nanocomposites	Hydrothermal synthesis and tubular sintering	ZT = 0.22 at 577 K	Enhanced thermoelectric figure-of-merit, reduced thermal conductivity	78
Ca <sub>3</sub> Co <sub>4</sub> O <sub>9</sub> +δ with SiC nanoparticles	Optimization strategy that involves the simultaneous optimization of two or more variables or objectives	Optimal ZT = 0.25 at 923 K	Substituting elements and dispersing silicon carbide nanoparticles	81
Composite thermoelectric materials (CuO) <sub>x</sub> (ZnO) <sub>1-x</sub>	Solid-state reaction	Power factor of 12.92 μW/mK <sup>2</sup> at 575 K	Variations in CuO content, alterations in the structural and electrical properties	86
Thermoelectric layers made of inorganic materials on single-walled carbon nanotubes (SWCNTs)	Electrodeposition	Improved thermoelectric efficiency	Utilization of inorganic coatings, enhanced power factor	87
SnTe-Cu <sub>2</sub> SnTe <sub>3</sub> nanocomposites	SnTe precursor lacking thiols	Peak ZT = 1.04 at 823 K	Increased electrical conductivity, decreased lattice thermal conductivity	99
MnTe	MA + SPS, Na doping	ZT > 1.0 at 873 K	Sodium doping, high power factor	101
FeNbSb (heavy-band HF-doped)	High HF content, figure-of-merit	ZT ≈ 1.5 at 1200 K	Optimized power factor; suppressed thermal conductivity	102
Ag-doped ZnSb	In situ Ag <sub>3</sub> Sb nanostructures	ZT = 1.15 at 670 K	Optimized carrier concentration, reduced thermal conductivity	103

Table 1. continued

Material	Synthesis/Methods	Thermoelectric Performance	Key Features/Contributing Factors	Ref.
RFeSb and MCoSb systems	Band engineering, solid solutions	Enhanced thermoelectric performance	Strategies: band engineering, solid solutions	104
PbSeTe/PbTe quantum-dot SLs	Molecular beam epitaxy	ZT = 3 (Bi-doped) at 550 K   ZT ≈ 1.1 (Na-doped) at 300 K	High ZT due to quantum-dot super lattices	105
SnSe (Ag-doped)	Transport properties, Ag doping	ZT = 0.6 at 750 K	Anisotropic/hysteresis-bearing transport properties	106
Elemental tellurium	Density functional theory, transport	ZT = 0.31 at room temp   ZT = 0.56 at 500 K	Anisotropic Fermi surface, distinct band structure	107
Cu <sub>3</sub> Sb <sub>0.975</sub> Sn <sub>0.025</sub> Se <sub>4</sub>	Sn-doping, crystal structure	ZT = 0.75 at 673 K	Tunable electrical conductivity, reduced lattice thermal conductivity	108
Cu-doped SnSe	Fusion method + SPS, Cu <sub>2</sub> Se phase	ZT ≈ 0.7 at 773 K	Cu <sub>2</sub> Se phase, intrinsic nanostructure formation	109
Mg <sub>3</sub> Si <sub>2</sub> Te <sub>6</sub> (Si-based)	First-principles + Boltzmann	ZT > 1 above 600 K	Low lattice thermal conductivity, direct band gap semiconductor	110

sequently, further investigation and exploration of ZnSb in this context are warranted.<sup>102</sup> This comprehensive review provides an overview of the notable progress made in improving the thermoelectric efficiency of p-type half-Heusler compounds, specifically focusing on the RFeSb and MCoSb systems. Various strategies, such as band engineering, solid solutions, and phonon scattering, have been employed to achieve these advancements. The review also discusses the crystal and electronic structure characteristics of these compounds and offers valuable insights into potential areas of future research for enhancing the thermoelectric properties of half-Heusler materials.<sup>103</sup> The thermoelectric performance of PbSeTe/PbTe quantum-dot super lattices (QDSLs) grown by molecular beam epitaxy (MBE) is significantly enhanced by the introduction of Bi-doping in the n-type region and Na-doping in the p-type region. These QDSLs demonstrate impressive figures of merit (ZT), with Bi-doped samples achieving a ZT value of 3 at a temperature of 550 K, while Na-doped samples exhibit a ZT value of approximately 1.1 at 300 K. These findings highlight the potential of these QDSLs for efficient thermoelectric applications.<sup>104</sup> The present study examines the transport properties of p-type polycrystalline SnSe doped with Ag, focusing on its anisotropic and hysteresis-bearing characteristics. The investigation reveals a noteworthy thermoelectric figure-of-merit (zT) peak value of 0.6 at a temperature of 750 K. This finding highlights the material's promise for thermoelectric applications, while also acknowledging the obstacles that need to be addressed.<sup>105</sup> By employing density functional theory and the Boltzmann transport equation, the analysis of the thermoelectric transport properties of elemental tellurium reveals its potential as a favorable p-type thermoelectric material. This potential arises from the anisotropic Fermi surface characteristics and unique electronic band structure of tellurium, resulting in a high figure-of-merit (zT) of 0.31 at room temperature and 0.56 at 500 K. These findings suggest that thermoelectric materials based on polychalcogenides could be developed with improved performance, as indicated by the enhanced zT values.<sup>106</sup> The introduction of Sn into the Sb position of the ternary chalcogenide Cu<sub>3</sub>SbSe<sub>4</sub> results in the development of a new p-type thermoelectric material, Cu<sub>3</sub>Sb<sub>0.975</sub>Sn<sub>0.025</sub>Se<sub>4</sub>. This material exhibits a significantly high ZT of 0.75 at a temperature of 673 K. This enhanced performance can be attributed to the crystal structure of Cu<sub>3</sub>Sb<sub>0.975</sub>Sn<sub>0.025</sub>Se<sub>4</sub>, which features a Cu/Se framework that allows for adjustable electrical conductivity. Additionally, the presence of [SbSe<sub>4</sub>] tetrahedra in the crystal structure contributes to a reduction in lattice thermal conductivity and an increase in the Seebeck coefficient.<sup>107</sup> The synthesis of Cu-doped SnSe using a fusion method and subsequent spark plasma sintering results in a significant improvement in the zT at a temperature of 773 K, reaching approximately 0.7. The improvement is credited to the addition of a second phase, Cu<sub>2</sub>Se, and the formation of an intrinsic nanostructure. These findings suggest that Cu-doped SnSe holds great potential as a cost-effective and efficient p-type thermoelectric material.<sup>108</sup> The compound Mg<sub>3</sub>Si<sub>2</sub>Te<sub>6</sub>, which is based on silicon (Si), has been studied using ab initio and Boltzmann transport computations. These investigations have revealed that Mg<sub>3</sub>Si<sub>2</sub>Te<sub>6</sub> is a direct bandgap semiconductor with favorable valence bands and a high degree of valley degeneracy. Additionally, the weak bonding of the magnesium (Mg) atoms in Mg<sub>3</sub>Si<sub>2</sub>Te<sub>6</sub> results in low phonon group velocities and high anharmonicity. As a consequence,

the compound exhibits a low lattice thermal conductivity and excellent electronic transport properties. Specifically, the p-type  $\text{Mg}_3\text{Si}_2\text{Te}_6$  material achieves a  $zT$  greater than 1 at temperatures above 600 K. Along the cross-plane direction, it reaches a  $zT$  value of 2.0 at 900 K. These findings provide valuable insights for the design of silicon-based thermoelectric materials.<sup>109</sup>

**3.6. Thermoelectric Materials Doped with n-Type Impurities.** Novel n-type organic thermoelectric materials, which are based on diradicaloids like 2DQQT-S and 2DQQT-Se, have been effectively developed and produced. These materials demonstrate remarkable resistance to air degradation and possess elevated electrical conductivity. These characteristics underscore their potential as viable options for the realization of organic thermoelectric materials that are both stable in air and exhibit superior performance.<sup>110</sup> The application of first-principles calculations demonstrates that an ultrathin nanosheet composed of  $\text{Bi}_2\text{O}_2\text{Se}$  displays a remarkably high  $ZT$  of 3.35 at a temperature of 800 K, when subjected to optimal n-type doping. This  $ZT$  value surpasses the  $ZT$  value of 2.6 observed in bulk  $\text{SnSe}$ , thereby highlighting the substantial potential of reduced dimensions in augmenting the thermoelectric performance. This finding is supported by reference 111. This study investigates the impact of n-type dopants on the enhancement of thermoelectric properties in Zintl antimonides, with a specific focus on n-type  $\text{Mg}_3\text{Sb}_{1.5}\text{Bi}_{0.5}$ . The analysis is conducted based on principles derived from electronegativity, which demonstrate that the efficiency of chalcogen dopants increases as the electronegativity difference decreases. This leads to improvements in carrier concentration and mobility, providing valuable insights for the purposeful design of materials.<sup>112</sup> This review highlights the importance of addressing various factors, including n-doping efficiency, charge carrier mobility, and stability, in order to enhance the conductivity of n-type conducting polymers for improved thermoelectric performance. The objective is to provide valuable guidance for the advancement of polymer thermoelectric materials with superior performance.<sup>113</sup> The present study provides a thorough examination of recent progress made in the field of n-type conjugated polymer thermoelectric materials. It specifically focuses on the challenges associated with enhancing n-doping efficiency and electron transport. Additionally, the review offers valuable insights into the relationship between material structure and performance, which can serve as a valuable guide for the design of future thermoelectric materials. (Citation 114) This paper provides a thorough analysis of the most recent advancements in n-type organic thermoelectric (OTE) materials and systems. It highlights the necessity for additional research efforts aimed at improving the stability and performance of these materials, particularly for thermoelectric applications that require high efficiency.<sup>115</sup> The present study presents the introduction of air-stable n-type single-walled carbon nanotubes that have been doped with weak electron donors. This research showcases the considerable potential of these nanotubes for flexible thermoelectric applications and the recovery of waste heat under ambient settings.<sup>116</sup> The potential of Te-doped  $\text{Mg}_3\text{Sb}_{1.5}\text{Bi}_{0.5}$  as an economically viable n-type thermoelectric material with remarkable performance is showcased due to its distinctive multivalley band behavior. This material exhibits high thermoelectric efficiency, making it suitable for waste heat recovery applications at low to intermediate temperatures.<sup>117</sup> The potential of Tm and Ce as effective n-type dopants in

$\text{Mg}_3\text{Sb}_2$ -based Zintl compounds is proved using defect calculations based on first principles. This research reveals that these compounds have intriguing characteristics as thermoelectric materials, exhibiting good thermoelectric performance and efficient carrier production.<sup>118</sup> The enhancement of electron mobility and electrical conductivity in n-type polymers BDPPV, ClBDPPV, and FBDPPV is achieved through the integration of halogen atoms into their polymer backbones, coupled with effective doping using N-DMBI. Notably, FBDPPV demonstrates the highest thermoelectric power factor reported to date among solution-processable n-type conjugated polymers.<sup>119</sup> The utilization of supramolecular salt-functionalized n-doped ladder-type conducting polymers has demonstrated exceptional resistance to air degradation, thus resolving a persistent obstacle in the advancement of stable n-type organic thermoelectric devices for energy harvesting.<sup>120</sup> The use of GaSb doping in PbS results in the convergence of the conduction band, hence improving the electrical transport characteristics and attaining an unprecedented average power factor and figure-of-merit for n-type PbS-based thermoelectric materials.<sup>121</sup> The Janus ZrSSe monolayer demonstrates exceptional thermoelectric capabilities when subjected to biaxial strain. This strain-induced band degeneracy and phonon suppression contribute to its high-power factor and figure of merit values. Consequently, the Janus ZrSSe monolayer shows great potential as a viable option for adjustable thermoelectric applications.<sup>122</sup>

As seen in Figure 30, both n- and p-type elements are required for a thermoelectric generator. Most of the time,

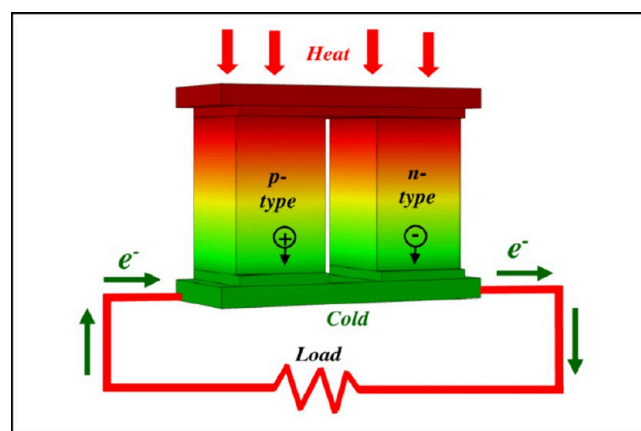


**Figure 30.** Thermoelectric generator shown in a schematic figure, including both n-type and p-type components.<sup>123</sup> Copyright Mohammed et al. *A review of thermoelectric p-type  $\text{Ca}_3\text{Co}_4\text{O}_9$  nanostructured ceramics for exhaust energy recovery*, 2017.

semiconductors make up these components. When a heat source is placed on one side of the generator and a heat sink on the other, a temperature gradient is formed. With fewer electrons than n-type elements, p-type elements have “holes” in their structure. When there is a temperature differential between the n-type and p-type sides of the generator, electrons move from the hot side to the cold side, resulting in electric current. The direct conversion of heat energy into electricity is made possible by the thermoelectric generator via the Seebeck effect. Small electronics or energy systems could be augmented by this electricity. In situations where there is a large temperature differential, simple and adaptable thermoelectric generators may be useful.

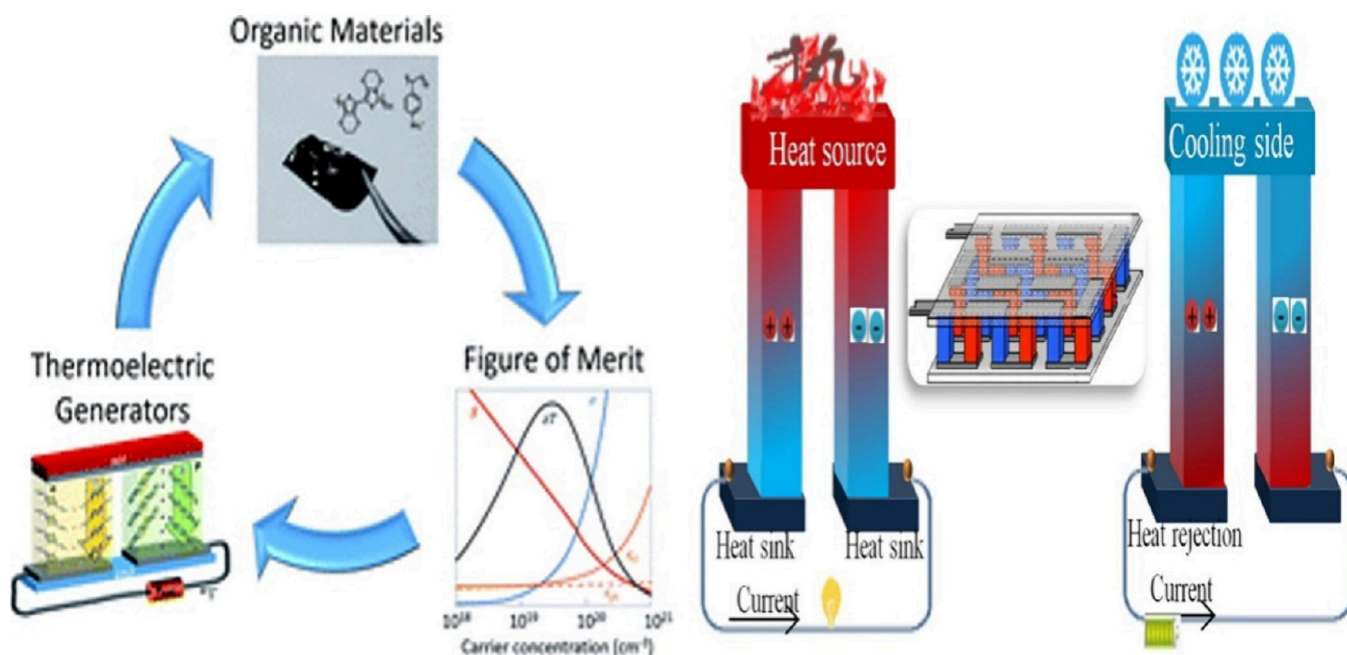


Figure 31. Schematic diagram of organic thermoelectric materials.<sup>136</sup> Copyright *Journal of Materials Chemistry A* 2020, 8, 7495–7507.

### 3.7. Materials with an Organic Thermoelectric Component.

Organic thermoelectric materials refer to a wide array of carbon-based compounds and polymers that have the capacity to transform thermal energy into electrical energy.<sup>124</sup> The molecular flexibility and tunability of organic materials are the defining features that offer researchers a distinct platform for customizing their electrical and thermal properties.<sup>125</sup> Through meticulous manipulation of the molecular architecture, establishment of efficient charge transport routes, and precise modulation of doping concentrations, researchers possess the ability to enhance the thermoelectric efficiency of organic substances.<sup>126</sup> The mechanical flexibility of organic thermoelectric materials is considered to be a significant benefit.<sup>127</sup> In contrast to inorganic materials, organic materials possess the capacity to be manufactured into flexible and adaptable structures, rendering them well-suited for applications that prioritize shape adaptation.<sup>128</sup> Wearable electronics have the ability to utilize organic thermoelectric materials in order to generate electricity from the heat produced by the human body.<sup>129</sup> This advancement could lead to the development of self-sustaining electronic textiles and health monitoring systems.<sup>130</sup> Nevertheless, organic materials present a distinct set of problems.<sup>131</sup> These materials frequently have reduced electrical conductivity and increased heat resistance due to their intricate molecular architectures and less robust intermolecular interactions.<sup>132</sup> The aforementioned characteristics have a detrimental impact on thermoelectric efficiency, since they can compromise the temperature gradient across the material.<sup>133</sup> The difficulties at hand are being actively investigated by researchers through the exploration of novel approaches, including molecular doping, hierarchical nano structuring, and the improvement of charge carrier mobility.<sup>134</sup> Organic thermoelectric materials exhibit potential for low-power applications and situations that necessitate flexibility, notwithstanding the obstacles they face.<sup>135</sup>

As seen in Figure 31, the organic material's structure is shown in the organic thermoelectric materials schematic

diagram, which emphasizes the n-type and p-type semi-conducting regions that are crucial for the Seebeck effect. In many cases, the graphic will show a heat source and a heat sink to illustrate the required temperature differential for the transformation of thermal energy into electrical current. The electric current generated when electrons and holes pass through a material is represented by the movement of charge carriers, which may be seen via connecting conductors. Electric current, an external load, and, optionally, a cooling system to maintain the necessary temperature differential are all shown in the image. Organic thermoelectric materials convert heat energy into electricity by means of the Seebeck effect, as shown in this schematic.

### 3.8. Discussion Pertaining to Inorganic Thermoelectric Materials.

In contrast, inorganic thermoelectric materials are comprised of crystalline solids that are formed of elements or compounds that are not carbon-based.<sup>137</sup> The efficient transfer of charge carriers and the resulting enhanced electrical conductivity in these materials can be attributed to their regular and ordered atomic organization.<sup>138</sup> The inherent advantage of inorganic materials adds to a higher level of thermoelectric efficiency when compared to organic materials. Furthermore, it has been observed that inorganic materials generally display reduced thermal resistance, which enables them to sustain a greater temperature gradient. Consequently, this characteristic facilitates the more efficient conversion of heat energy into electrical energy.<sup>139</sup> One of the main obstacles encountered with inorganic thermoelectric materials is to their comparatively elevated thermal conductivity.<sup>140</sup> The presence of low thermal resistance is advantageous; nevertheless, an excessive level of thermal conductivity can result in substantial heat dissipation and a decrease in the overall efficiency of thermoelectric devices.<sup>141</sup> Scholars are currently investigating diverse approaches to address this matter, including the use of nanostructuring and alloying and the utilization of intricate crystal structures to disperse phonons, which serve as the main agents of heat transfer.<sup>142</sup> In high-power circumstances where waste heat recovery and power generation are crucial,

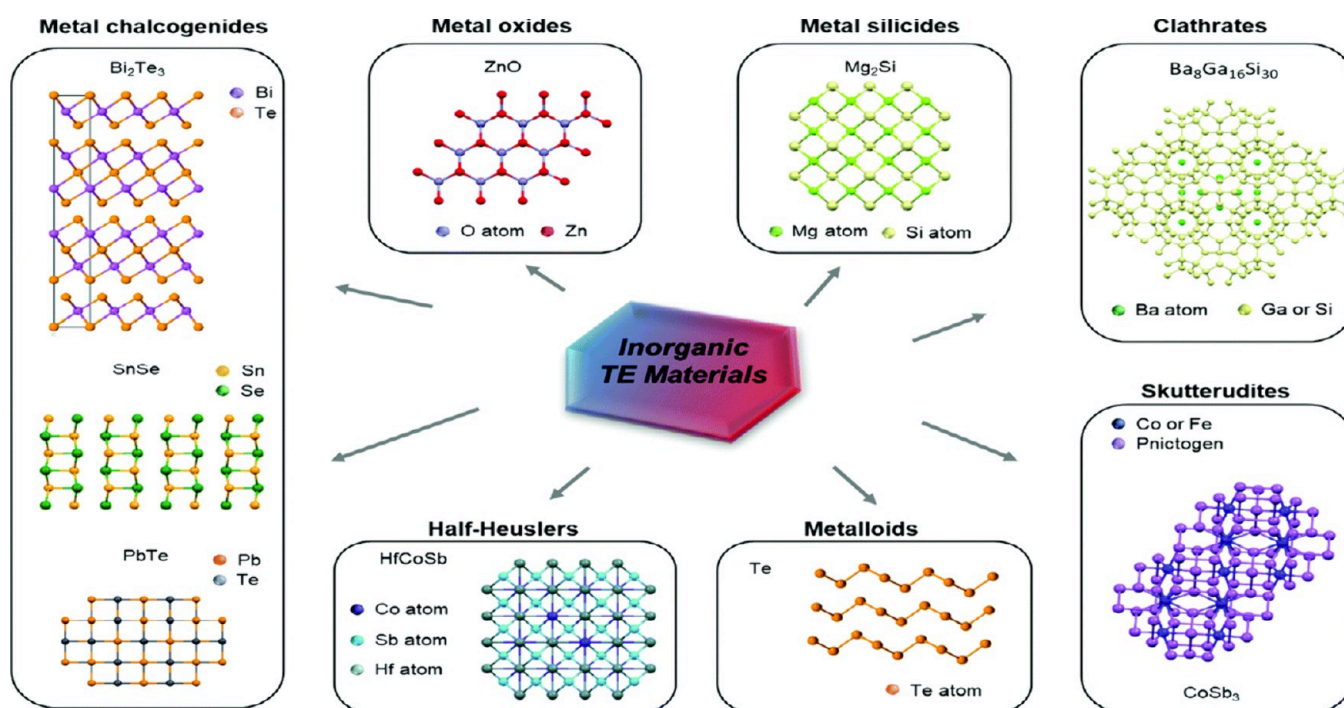


Figure 32. Examples of inorganic thermoelectric materials.<sup>145</sup> Copyright *Chemical Society Reviews* 2022, 51, 485–512.

Table 2. Comparative Analysis of Thermoelectric Properties in Organic and Inorganic Materials

Characteristics	Organic Thermoelectric Materials	Inorganic Thermoelectric Materials	Ref
Heat-to-electricity conversion	Process of converting heat into electricity via the use of molecular flexibility and tunability.	Conversion of heat to electricity with efficient charge carrier transport and ordered atomic arrangement.	124
Tailoring properties	With the use of molecular engineering and doping, properties may be modified.	Properties affected by alloying, nanostructuring, and crystal structure.	125
Mechanical flexibility	High mechanical flexibility, ideal for wearable technology and form-fitting materials.	Typically less flexible and more appropriate for stiff constructions.	127
Electrical conductivity	Often exhibit lower electrical conductivity due to complex molecular structures.	Higher electrical conductivity due to ordered atomic arrangement.	132
Thermal resistance	Higher thermal resistance, leading to reduced thermoelectric efficiency.	Lower thermal resistance, enabling better maintenance of temperature gradient.	139
Thermal conductivity	Reduce thermal conductivity to prevent heat loss.	Higher heat conductivity, which may make thermoelectric efficiency difficult.	141
Applications	Wearable electronics, self-sustaining textiles, and low-power applications.	Waste heat recovery, high-power applications, and the automotive and aerospace industries.	130
Challenges	Higher heat resistance, lower electrical conductivity.	Potential for increased heat loss due to higher thermal conductivity.	132
Strategies for improvement	Improved charge carrier mobility, molecular doping, and hierarchical nano structuring.	Phonons may be scattered by nanostructuring, alloying, and complicated crystal formations.	134
Overall suitability	Essential for applications that prioritize flexibility.	Waste heat recovery is suitable for situations involving high power.	135

inorganic thermoelectric materials demonstrate significant potential for appealing applications.<sup>143</sup> Various industries, including manufacturing, automotive, and aerospace, have the opportunity to utilize these materials in order to transform surplus heat into valuable electricity. This application has the potential to enhance energy efficiency and mitigate environmental consequences.<sup>144</sup>

As seen in Figure 32, a diverse range of inorganic thermoelectric materials have been created that effectively transform heat into electricity (Table 2). Separate sections within the temperature ranges enable the presentation of items that have undergone extensive examination within those regions. The 300–450 K range is where you can find notable examples like  $\text{Bi}_2\text{Te}_3$ ,  $\text{Sb}_2\text{Te}_3$ , and  $\text{Ag}_2\text{Se}$ . Common choices for transitioning to the 450–900 K range include  $\text{PbTe}$ ,  $\text{PbSe}$ , half-Heuslers, and skutterudites. Materials such as  $\text{SnSe}$  and  $\text{SiGe}$  have superior thermoelectric properties when exposed to

temperatures over 750 K. Various synthesis methods, including solid-state methodologies and solution-based wet-chemistry processes, are shown to highlight the versatility in modifying particle characteristics. This comprehensive analysis emphasizes the significance of inorganic thermoelectric materials, which are important to the development of energy conversion technologies in several domains.

#### 4. APPLICATION OF THERMOELECTRIC MATERIALS

Thermoelectric materials have been used in several sectors for purposes such as energy harvesting, waste heat recovery, and thermal management. Below are instances of practical use of thermoelectric materials in various sectors.

**4.1. Vehicle Market.** Thermoelectric generators (TEGs) are being studied to use and convert waste heat from the exhaust system into electrical energy, with the possibility of improving the fuel efficiency of vehicles.

**4.2. Thermal Management of Electronic Devices.** Electronic equipment, including specific refrigeration units in trucks and containers for temperature-sensitive commodities, made use of thermoelectric coolers.

**4.3. Wearable Developments.** Thermoelectric generators were included in a few wearable gadgets in order to transform the user's thermal energy into usable electricity for low-power sensors and displays.

**4.4. Use in the Aerospace Industry.** Thermoelectric materials were used in space missions to generate electricity. Radioisotope thermoelectric generators (RTGs) transform heat from decaying radioactive isotopes into electrical power for spacecrafts using thermoelectric principles.

**4.5. Utilization of Excess Heat from Industrial Processes.** Thermoelectric materials were used by industries that include high-temperature processes, such as steel and glass manufacture, to capture and transform waste heat into power for on-site consumption.

**4.6. Use in the Military.** A potential solution that the military investigated was thermoelectric generators, which may provide electricity to sensors or equipment in areas without access to more conventional power sources.

**4.7. Electronics for Personal Use.** Certain camping stoves and portable chargers use thermoelectric generators to transfer heat from the stove into electrical energy for the purpose of charging electronic gadgets.

## 5. LIMITATIONS OF NANOCOMPOSITE THERMOELECTRIC MATERIALS

Composite thermoelectric materials have a lot of potential for improving thermoelectric device efficiency, but they also come with a lot of problems and restrictions. Giving a fair assessment will help readers make sense of the technology as it is right now and identify gaps that need filling with further studies. The following are some restrictions.

**5.1. Misalignment of Thermal Conductivity.** The challenge is in achieving a balance between electrical conductivity and thermal conductivity. Often, improvements in one attribute are attained at the expense of the other. Maximizing these attributes is crucial for attaining the best possible thermoelectric performance.

**5.2. Difficulty of Fabrication.** Precise manipulation of the composition, morphology, and interfaces is crucial throughout the intricate manufacturing processes of composite materials. Attaining component consistency is challenging, and any deviations might potentially impact overall performance.

**5.3. Factors Relating to Budget.** The production of composite thermoelectric materials may result in higher expenses in comparison to traditional materials. This characteristic might impede their widespread use, especially in large-scale applications where cost-effectiveness is crucial.

**5.4. Problems with Adaptability.** Expanding the manufacturing of composite thermoelectric materials for commercial use may present difficulties. Procedures that show efficacy in the laboratory may not readily transition to industrial-scale production.

**5.5. Restricted Selection of Materials.** Composite thermoelectric materials have a restricted selection of materials. A continuing problem in the industry is the search for novel materials that display the appropriate mix of features.

**5.6. Operation in Very Hot Environments.** Some composite materials may experience a deterioration in

performance at severe temperatures, which restricts their usefulness in specific high-temperature settings.

**5.7. Familiarizing Oneself with and Mastering Interfaces.** The interactions between distinct components in composite materials have a crucial impact. Further study is necessary to comprehend and regulate these interactions in order to improve thermoelectric performance.

## 6. THEORETICAL AND EXPERIMENTAL ADVANCES

**6.1. Theoretical Outlook.** The field of thermoelectric materials offers exciting avenues for future exploration and innovation:

1. Nanocomposites and nanostructures: investigating advanced nanocomposites and nanomaterials could lead to enhanced thermoelectric properties by optimizing phonon scattering and charge carrier mobility.
2. Quantum design: leveraging computational materials science to tailor material properties at the quantum level offers the potential to design high-performance thermoelectric materials with precision.
3. 2D and layered materials: exploring the thermoelectric behavior of emerging 2D and layered materials, like graphene and transition metal dichalcogenides, holds promise for flexible and efficient energy conversion.
4. Advanced manufacturing: developing scalable manufacturing techniques, such as additive manufacturing, can facilitate the production of thermoelectric devices with tailored geometries and improved performance.
5. Hybrid and multifunctional materials: integrating thermoelectric materials with other energy conversion technologies and functional materials opens avenues for versatile applications in energy harvesting.
6. Sustainable sourcing: researching sustainable and earth-abundant materials can lead to eco-friendly alternatives, ensuring the long-term viability of thermoelectric technology.
7. Real-world applications: collaborating with industries to bridge the gap between research and commercialization can drive the integration of thermoelectric devices in sectors like automotive, aerospace, and electronics.

### 6.2. Experimental Outlook.

1. Improving the scattering of phonons and the mobility of charge carriers may be achieved by precisely altering the mix of Bi<sub>2</sub>Te<sub>3</sub> and Sb<sub>2</sub>Te<sub>3</sub> in nanocomposite thermoelectric materials (e.g., (Bi<sub>2</sub>Te<sub>3</sub>)<sub>0.8</sub>(Sb<sub>2</sub>Te<sub>3</sub>)<sub>0.2</sub>). Determine how well these changes worked by taking readings of the thermal conductivity and Seebeck coefficient. Similarly, nanocomposites made from carefully measured amounts of silicon (Si) and germanium (Ge) may increase thermoelectric performance by combining the best properties of the two elements.
2. Synthesize and characterize new thermoelectric materials found in computational models; next, modify factors like doping levels and crystal structures to get the quantum characteristics you want, and you'll have experimentally implemented quantum design. Synthesize semiconductor quantum dots, such as lead selenide (PbSe) or silicon (Si) and then experiment with different doping levels (e.g., phosphorus or boron) to maximize thermoelectric performance by manipulating charge carriers at the quantum level. Produce thin layers of topological insulators, such as bismuth selenide (Bi<sub>2</sub>Se<sub>3</sub>) or bismuth

telluride (Bi<sub>2</sub>Te<sub>3</sub>), and investigate how the thickness and surface states impact the thermoelectric properties, taking use of the quantum characteristics of these substances.

- Experiment: fabricate graphene-based devices with controlled geometry and study their thermoelectric performance by measuring Seebeck coefficients and electrical conductivities. Investigate possible layer-to-layer synergies by building van der Waals heterostructures and stacking various 2D materials like graphene and hexagonal boron nitride (h-BN). Then, measure thermoelectric performance. The nanowires of iron (Fe) oxide are included inside a matrix of an organic polymer that is obtained from sustainable sources, such as biobased polyethylene.
- To improve performance, decrease heat conductivity, and guarantee compatibility with sustainable and scalable production, this composite blends efficient SnSe with an eco-friendly conducting polymer and sustainable nanofillers.
- Use Earth-based components and compounds to develop eco-friendly thermoelectric materials. Test their thermoelectricity in a lab. Tin, which is abundant on Earth, is the major component of SnS, and carbon nanotubes boost its electrical conductivity. This composite should be thermoelectricity-efficient, sustainable, and scalable for future trials.

## 7. CONCLUSION

In conclusion, this comprehensive review offers a thorough analysis of the most recent advancements in the field of thermoelectric materials. This work investigates many tactics, including codoping, nanoparticle inclusion, and structural changes, which play a vital role in improving the efficiency of these materials. This statement highlights the significant capacity of inorganic materials in efficiently harnessing waste heat while also emphasizing the versatility of organic materials, particularly in the context of wearable technology. This review paper highlights the essential significance of thermoelectric materials in promoting energy sustainability and advancing technology, focusing on crucial aspects such as the thermoelectric figure-of-merit ( $ZT$ ) and thermal conductivity. Based on these observations, it is apparent that the continuous research and advancements in this subject have the potential to make substantial contributions to the domains of energy preservation and ecological responsibility.

## AUTHOR INFORMATION

### Corresponding Author

Ghulam Rasool – Faculty of Material and Manufacturing, Beijing University of Technology, Beijing 100124, China; Department of Mechanical Engineering, Lebanese American University, Beirut, Lebanon; [orcid.org/0000-0002-5880-9553](https://orcid.org/0000-0002-5880-9553); Email: [grasool@bjut.edu.cn](mailto:grasool@bjut.edu.cn)

### Authors

Wajid Hussain – Faculty of Material and Manufacturing, Beijing University of Technology, Beijing 100124, China  
Salem Algarni – Mechanical Engineering Department, College of Engineering, King Khalid University, Abha 9004, Saudi Arabia  
Hasan Shahzad – Faculty of Energy and Power Engineering, School of Chemical Engineering and Energy Technology,

Dongguan University of Technology, Dongguan, Guangdong, China

Mujahid Abbas – Faculty of Material and Manufacturing, Beijing University of Technology, Beijing 100124, China

Talal Alqahtani – Mechanical Engineering Department, College of Engineering, King Khalid University, Abha 9004, Saudi Arabia

Kashif Irshad – Interdisciplinary Research Centre for Sustainable Energy Systems (IRC-SES), Research Institute, King Fahd University of Petroleum and Minerals (KFUPM), Dhahran 31261, Saudi Arabia

Complete contact information is available at:

<https://pubs.acs.org/10.1021/acsomega.3c07758>

## Notes

The authors declare no competing financial interest.

## ACKNOWLEDGMENTS

The authors extend their appreciation to the Deanship of Scientific Research at King Khalid University for funding this work through a small group Research Project under grant number RGP.1/97/44.

## REFERENCES

- Gaultois, M. W. Perspective: Web-based machine learning models for real-time screening of thermoelectric materials properties. *Appl. Mater.* **2016**, DOI: [10.1063/1.4952607](https://doi.org/10.1063/1.4952607).
- Yu, C.; Chau, K.T. Thermoelectric automotive waste heat energy recovery using maximum power point tracking. *Energy Conversion and Management* **2009**, *50*, 1506–1512.
- Kim, J.; et al. Wearable biosensors for healthcare monitoring. *Nature biotechnology* **2019**, *37*, 389–406.
- Chen, Z.-G.; Han, G.; Yang, L.; Cheng, L.; Zou, J.; et al. Nanostructured thermoelectric materials: Current research and future challenge. *Progress in Natural Science: Materials International* **2012**, *22*, 535–549.
- He, J.; Tritt, T. M. Advances in thermoelectric materials research: Looking back and moving forward. *Science* **2017**, *357*, No. eaak9997.
- Ando Junior, O. H.; et al. Proposal of a thermoelectric microgenerator based on seebeck effect to energy harvesting in industrial processes. *REPQJ* **2014**, *1*, 227.
- Nikam, A. N.; Hole, J. A. A Review on use of Peltier Effects. *International Journal of Science, Spirituality, Business, And Technology (IJSSBT)* **2014**.
- Yushanov, S. P., et al. Multiphysics analysis of thermoelectric phenomena. *Seventh Annual Conference on Multiphysics Modeling and Simulation. Proceedings of the 2011 COMSOL Conference*, Boston, USA, 2011.
- Hamid Elsheikh, M.; Shnawah, D. A.; Sabri, M. F. M.; Said, S. B. M.; Haji Hassan, M.; Ali Bashir, M. B.; Mohamad, M.; et al. A review on thermoelectric renewable energy: Principal parameters that affect their performance. *Renewable and sustainable energy reviews* **2014**, *30*, 337–355.
- Snyder, G. J.; Toberer, E. S. Complex thermoelectric materials. *Nature materials* **2008**, *7*, 105–114.
- Russ, B.; et al. Organic thermoelectric materials for energy harvesting and temperature control. *Nat. Rev. Mater.* **2016**, *1*, 1–14.
- Taroni, P. J.; Hoces, I.; Stingelin, N.; Heeney, M.; Bilotti, E.; et al. Thermoelectric materials: A brief historical survey from metal junctions and inorganic semiconductors to organic polymers. *Isr. J. Chem.* **2014**, *54*, 534–552.
- He, Y.; et al. Multifunctional organohydrogel with rambutan-like microstructure for waste heat recovery and intelligent sensing. *Compos. Sci. Technol.* **2023**, *242*, 110163.

- (14) Mukherjee, M.; Srivastava, A.; Singh, A. K. Recent advances in designing thermoelectric materials. *Journal of Materials Chemistry C* **2022**, *10*, 12524.
- (15) Channegowda, M.; et al. Comprehensive insights into synthesis, structural features, and thermoelectric properties of high-performance inorganic chalcogenide nanomaterials for conversion of waste heat to electricity. *ACS Appl. Energy Mater.* **2022**, *5*, 7913–7943.
- (16) Wang, Z.-L.; Funada, T.; Onda, T.; Chen, Z.-C.; et al. Knowledge extraction and performance improvement of Bi<sub>2</sub>Te<sub>3</sub>-based thermoelectric materials by machine learning. *Materials Today Physics* **2023**, *31*, 100971.
- (17) Chen, G.; et al. Electronic textiles for wearable point-of-care systems. *Chem. Rev.* **2022**, *122*, 3259–3291.
- (18) Alghamdi, H.; et al. Transient numerical simulations in innovative thermoelectric power: A comprehensive study on material segmentation and cross-section design for multi-faceted excellence. *Case Studies in Thermal Engineering* **2023**, *52*, 103684.
- (19) Saha, M.; et al. A review of thermoelectric generators for waste heat recovery in marine applications. *Sustainable Energy Technologies and Assessments* **2023**, *59*, 103394.
- (20) Jouhara, H.; et al. Waste heat recovery technologies and applications. *Thermal Science and Engineering Progress* **2018**, *6*, 268–289.
- (21) Mishra, R. K., et al. Mxene: The Multifunctional Two-Dimensional Material for Next-Generation Devices. DOI: 10.13140/RG.2.2.10142.10566
- (22) Rani, M.; et al. Recent advancement and challenges in multifunctional carbon nanotube buckypaper and its composites for energy storage and conversion applications. *Journal of Energy Storage* **2023**, *73*, 109063.
- (23) Alghamdi, H.; et al. From sunlight to power: Enhancing 4E performance with two-stage segmented thermoelectric generators in concentrated solar applications. *Journal of Cleaner Production* **2023**, *429*, 139314.
- (24) Singh, B. S. B. Thermoelectric Generators: Design, Operation, and Applications. *New Materials and Devices for Thermoelectric Power Generation*; IntechOpen, 2023.
- (25) Gallagher, J. B. *Synthesis of nanostructured materials with potential renewable energy generation applications*; Diss. University of Glasgow, 2015.
- (26) Beretta, D.; et al. Thermoelectrics: From history, a window to the future. *Materials Science and Engineering: R: Reports* **2019**, *138*, 100501.
- (27) Channegowda, M.; et al. Comprehensive insights into synthesis, structural features, and thermoelectric properties of high-performance inorganic chalcogenide nanomaterials for conversion of waste heat to electricity. *ACS Appl. Energy Mater.* **2022**, *5*, 7913–7943.
- (28) Liu, W.-D.; et al. Promising and eco-friendly Cu<sub>2</sub>X-based thermoelectric materials: progress and applications. *Adv. Mater.* **2020**, *32*, 1905703.
- (29) Jin, Z.; et al. Thermoelectric properties and service stability of Ag-containing Cu<sub>2</sub>Se. *Materials Today Physics* **2021**, *21*, 100550.
- (30) Cai, Y.; et al. Thermoelectric cooling technology applied in the field of electronic devices: Updated review on the parametric investigations and model developments. *Applied Thermal Engineering* **2019**, *148*, 238–255.
- (31) Chen, G.; et al. Recent developments in thermoelectric materials. *International materials reviews* **2003**, *48*, 45–66.
- (32) LeBlanc, S.; et al. Material and manufacturing cost considerations for thermoelectrics. *Renewable and Sustainable Energy Reviews* **2014**, *32*, 313–327.
- (33) Borup, K. A.; et al. Measuring thermoelectric transport properties of materials. *Energy Environ. Sci.* **2015**, *8*, 423–435.
- (34) Zhu, T.; et al. Compromise and synergy in high-efficiency thermoelectric materials. *Advanced materials* **2017**, *29*, 1605884.
- (35) Liao, W.-W.; et al. Realizing Bi-doped  $\alpha$ -Cu<sub>2</sub>Se as a promising near-room-temperature thermoelectric material. *Chem. Eng. J.* **2019**, *371*, 593–599.
- (36) Liu, W.-D.; et al. Promising and eco-friendly Cu<sub>2</sub>X-based thermoelectric materials: progress and applications. *Adv. Mater.* **2020**, *32*, 1905703.
- (37) Jin, Z.; et al. Thermoelectric properties and service stability of Ag-containing Cu<sub>2</sub>Se. *Materials Today Physics* **2021**, *21*, 100550.
- (38) Yang, D. Atomic mechanism of ionic confinement in the thermoelectric Cu<sub>2</sub>Se based on a low-cost electric-current method. *Cell Rep. Phys. Sci.* **2021**, *2*, 100345.
- (39) Choo, S.; et al. Cu<sub>2</sub>Se-based thermoelectric cellular architectures for efficient and durable power generation. *Nat. Commun.* **2021**, *12*, 3550.
- (40) Li, L.; et al. Maximizing phonon scattering efficiency by Cu<sub>2</sub>Se alloying in AgCuTe thermoelectric materials. *Journal of Materials Chemistry A* **2022**, *10*, 6701–6712.
- (41) Nieroda, P.; et al. Influence of DC and AC current in the SPS sintering process on homogeneity of thermoelectric properties of Cu<sub>2</sub>S and Cu<sub>2</sub>Se. *Ceram. Int.* **2023**, *49*, 9681–9690.
- (42) Rudradawong, C.; et al. Enhanced thermoelectric properties of Cu<sub>2</sub>Se via Sb doping: An experimental and computational study. *J. Eur. Ceram. Soc.* **2023**, *43*, 401–406.
- (43) Mangavati, S.; et al. The role of hetero-interface structures in enhancing the power factor of Cu<sub>2</sub>Se/x% Y<sub>2</sub>O<sub>3</sub> composite thermoelectric materials. *Mater. Res. Bull.* **2023**, *166*, 112362.
- (44) Purushottam Bhat, C.; et al. Investigations on Bi Doped Cu<sub>2</sub>Se Prepared by Solid State Reaction Technique for Thermoelectric Applications. *Energies* **2023**, *16*, 3010.
- (45) Zhao, H.; et al. A Self-Independent Binary-Sublattice Construction in Cu<sub>2</sub>Se Thermoelectric Materials. *Adv. Funct. Mater.* **2023**, *33*, 2304663.
- (46) Long, Z.; et al. Band Engineering of the Second Phase to Reach High Thermoelectric Performance in Cu<sub>2</sub>Se-Based Composite Material. *Adv. Mater.* **2023**, *35*, 2210345.
- (47) Cai, X.; et al. Valence Band Structure Degeneracy Enhanced Thermoelectric Performance in  $\beta$ -Cu<sub>2</sub>Se. *J. Phys. Chem. C* **2023**, *127*, 5576–5583.
- (48) Wang, X.; Tabarraei, A. Phonon thermal conductivity of monolayer MoS<sub>2</sub>. *Appl. Phys. Lett.* **2016**, DOI: 10.1063/1.4949561.
- (49) Zhang, Z.; et al. A theoretical prediction of super high-performance thermoelectric materials based on MoS<sub>2</sub>/WS<sub>2</sub> hybrid nanoribbons. *Sci. Rep.* **2016**, *6*, 21639.
- (50) Xie, Y.; et al. Flexible thermoelectric nanogenerator based on the MoS<sub>2</sub>/graphene nanocomposite and its application for a self-powered temperature sensor. *Semicond. Sci. Technol.* **2017**, *32*, 044003.
- (51) Fattah-alhosseini, A.; Keshavarz, M. K.; Attarzadeh, F. A study on the electrochemical responses of p-type bismuth telluride-based thermoelectric materials in a 0.1 M NaCl solution: Comparing a nanocomposite with dispersed MoS<sub>2</sub> nanoparticles and a single-phase alloy. *J. Alloys Compd.* **2020**, *815*, 152371.
- (52) Jenisha, M. A.; Kavirajan, S.; Harish, S.; Archana, J.; Kamalabharathi, K.; Kumar, E. S.; Navaneethan, M.; et al. Interfacial engineering effect and bipolar conduction of Ni-doped MoS<sub>2</sub> nanostructures for thermoelectric application. *J. Alloys Compd.* **2022**, *895*, 162493.
- (53) Tang, D.; Dan, M.; Zhang, Y. High performance piezotronic thermoelectric devices based on zigzag MoS<sub>2</sub> nanoribbon. *Nano Energy* **2022**, *104*, 107888.
- (54) Yang, Y.; He, D.; Zhou, Y.; Wen, S.; Huang, H. Electronic and surface modulation of 2D MoS<sub>2</sub> nanosheets for an enhancement on flexible thermoelectric property. *Nanotechnology* **2023**, *34*, 195401.
- (55) Shalini, V.; et al. Enhancement of thermoelectric power factor via electron energy filtering in Cu doped MoS<sub>2</sub> on carbon fabric for wearable thermoelectric generator applications. *J. Colloid Interface Sci.* **2023**, *633*, 120–131.
- (56) Wang, J.; et al. Excellent thermoelectric properties of monolayer MoS<sub>2</sub>-MoSe<sub>2</sub> aperiodic superlattices. *Appl. Surf. Sci.* **2023**, *612*, 155914.

- (57) Jiang, D. High-Performance MoS<sub>2</sub>/SWCNT Composite Films for a Flexible Thermoelectric Power Generator. *ACS Appl. Mater. Interfaces* **2023**, *15*, 30495.
- (58) Jenisha, M. A.; Kavirajan, S.; Harish, S.; Kamalakannan, S.; Archana, J.; Senthil Kumar, E.; Wakiya, N.; Navaneethan, M. Multiple approaches of band engineering and mass fluctuation of solution-processed n-type Re-doped MoS<sub>2</sub> nanosheets for enhanced thermoelectric power factor. *J. Colloid Interface Sci.* **2024**, *653*, 1150–1165.
- (59) Suresh, P. C.; et al. Interfacial energy barrier tuning in MnO<sub>2</sub>/MoS<sub>2</sub>/Carbon fabric integrated with low resistance textrode for highly efficient wearable thermoelectric generator. *Carbon* **2024**, *218*, 118609.
- (60) Chaudhuri, S. Hydrostatic Pressure-Induced Anomalous Enhancement in the Thermoelectric Performance of Monolayer MoS<sub>2</sub>. *ACS Appl. Energy Mater.* **2023**, *6*, 11694.
- (61) Bat-Erdene, M.; et al. Elemental 2D Materials: Solution-Processed Synthesis and Applications in Electrochemical Ammonia Production. *Adv. Funct. Mater.* **2022**, *32*, 2107280.
- (62) Li, Y.; et al. Opportunities for cryogenic electron microscopy in materials science and nanoscience. *ACS Nano* **2020**, *14*, 9263–9276.
- (63) Siddiqui, J.; et al. Nanomaterials in smart packaging applications: a review. *Small* **2022**, *18*, 2101171.
- (64) Blackburn, J. L.; et al. Carbon-nanotube-based thermoelectric materials and devices. *Adv. Mater.* **2018**, *30*, 1704386.
- (65) Zhao, Y.; Dyck, J. S.; Burda, C. Toward high-performance nanostructured thermoelectric materials: the progress of bottom-up solution chemistry approaches. *J. Mater. Chem.* **2011**, *21*, 17049–17058.
- (66) Mazzio, K. A.; et al. P-Type-to-N-Type transition in hybrid Ag<sub>x</sub>Te/PEDOT: PSS thermoelectric materials via stoichiometric control during solution-based synthesis. *ACS Appl. Energy Mater.* **2020**, *3*, 10734–10743.
- (67) Kumari, N.; Dasgupta, T. Developing contacting solutions for n-type Mg<sub>3</sub>Sb<sub>2</sub>·5Bi<sub>2</sub>·5 based thermoelectric materials. *J. Alloys Compd.* **2023**, *944*, 169220.
- (68) Aridi, R.; et al. Thermoelectric power generators: state-of-the-art, heat recovery method, and challenges. *Electricity* **2021**, *2*, 359–386.
- (69) Tai, G.; Guo, W.; Zhang, Z. Hydrothermal synthesis and thermoelectric transport properties of uniform single-crystalline pearl-necklace-shaped PbTe nanowires. *Cryst. Growth Des.* **2008**, *8*, 2906–2911.
- (70) Chen, Z.; et al. Hydrothermal synthesized nanostructure Bi–Sb–Te thermoelectric materials. *Journal of alloys and compounds* **2014**, *588*, 384–387.
- (71) Zhou, J.; Chen, Z.; Sun, Z. Hydrothermal synthesis and thermoelectric transport properties of PbTe nanocubes. *Mater. Res. Bull.* **2015**, *61*, 404–408.
- (72) Shi, W.; et al. Hydrothermal synthesis and thermoelectric transport properties of Sb<sub>2</sub>Te<sub>3</sub>–Te heterogeneous nanostructures. *CrystEngComm* **2013**, *15*, 2978–2985.
- (73) Zhang, Y.; et al. Hydrothermal synthesis and thermoelectric properties of nanostructured Bi<sub>2</sub>·5Sb<sub>2</sub>·5Te<sub>3</sub> compounds. *Mater. Res. Bull.* **2011**, *46*, 760–764.
- (74) Jin, R.; et al. Hydrothermal synthesis and thermoelectric transport property of PbS–PbTe core–shell heterostructures. *New J. Chem.* **2012**, *36*, 2574–2579.
- (75) Yue, Z.; et al. Thermoelectric performance of hydrothermally synthesized micro/nano Cu<sub>2</sub>·xS. *Chem. Eng. J.* **2022**, *449*, 137748.
- (76) Xu, R.; et al. Nanostructured SnSe integrated with Se quantum dots with ultrahigh power factor and thermoelectric performance from magnetic field-assisted hydrothermal synthesis. *Journal of Materials Chemistry A* **2019**, *7*, 15757–15765.
- (77) Shyni, P.; Pradyumnan, P. P. Deep tuning of Bi<sub>2</sub>Te<sub>3</sub> nanostructures suitable for thermoelectric waste heat recovery: The impact of pH on crystal growth in hydrothermal synthesis. *Materials Science and Engineering: B* **2023**, *287*, 116090.
- (78) Bai, Y.; et al. Boosting the thermoelectric performance of n-type Bi<sub>2</sub>S<sub>3</sub> by compositing rGO. *J. Alloys Compd.* **2023**, *933*, 167814.
- (79) Szczech, J. R.; Higgins, J. M.; Jin, S. Enhancement of the thermoelectric properties in nanoscale and nanostructured materials. *J. Mater. Chem.* **2011**, *21*, 4037–4055.
- (80) Ma, Z.; et al. High thermoelectric performance of SnTe by the synergistic effect of alloy nanoparticles with elemental elements. *ACS Appl. Energy Mater.* **2019**, *2*, 7354–7363.
- (81) Xia, S.; et al. Influence of SiC dispersion and Ba (Sr) substitution on the thermoelectric properties of Ca<sub>3</sub>Co<sub>4</sub>O<sub>9</sub>+ $\delta$ . *Ceram. Int.* **2022**, *48*, 24859–24865.
- (82) Bellanger, P.; et al. Effect of microstructure on the thermal conductivity of nanostructured Mg<sub>2</sub>(Si, Sn) thermoelectric alloys: An experimental and modeling approach. *Acta Mater.* **2015**, *95*, 102–110.
- (83) Chen, J.-L.; et al. Strategy of Extra Zr Doping on the Enhancement of Thermoelectric Performance for TiZr<sub>x</sub>NiSn Synthesized by a Modified Solid-State Reaction. *ACS Appl. Mater. Interfaces* **2021**, *13*, 48801–48809.
- (84) Ma, Y.; Heijl, R.; Palmqvist, A. E. C. Composite thermoelectric materials with embedded nanoparticles. *J. Mater. Sci.* **2013**, *48*, 2767–2778.
- (85) Ikram, S.; et al. Effect of Al concentration on the structural and thermoelectric properties of ZnAlS alloy. *Inorg. Chem. Commun.* **2022**, *144*, 109908.
- (86) Ghazi, N.; Kadhim, A. Thermoelectric properties of solid state reaction-prepared ZnO based alloys with various CuO doping in (CuO)<sub>x</sub>(ZnO)<sub>1-x</sub>. *Solid State Commun.* **2023**, *361*, 115058.
- (87) Eguchi, R.; Hoshino, K.; Takashiri, M. Sb<sub>2</sub>Te<sub>3</sub> nanoparticle-containing single-walled carbon nanotube films coated with Sb<sub>2</sub>Te<sub>3</sub> electrodeposited layers for thermoelectric applications. *Sci. Rep.* **2023**, *13*, 5783.
- (88) Saini, S.; et al. Terbium ion doping in Ca<sub>3</sub>Co<sub>4</sub>O<sub>9</sub>: A step towards high-performance thermoelectric materials. *Sci. Rep.* **2017**, *7*, 44621.
- (89) Fujita, K.; Mochida, T.; Nakamura, K. High-temperature thermoelectric properties of Na<sub>x</sub>CoO<sub>2</sub>· $\delta$  single crystals. *Jpn. J. Appl. Phys.* **2001**, *40*, 4644.
- (90) Liu, W.; et al. New trends, strategies and opportunities in thermoelectric materials: a perspective. *Materials Today Physics* **2017**, *1*, 50–60.
- (91) Brown, S. R.; et al. Yb<sub>14</sub>MnSb<sub>11</sub>: New high efficiency thermoelectric material for power generation. *Chemistry of materials* **2006**, *18*, 1873–1877.
- (92) Mikami, M.; et al. High-temperature thermoelectric properties of single-crystal Ca<sub>3</sub>Co<sub>2</sub>O<sub>6</sub>. *Journal of applied physics* **2003**, *94*, 6579–6582.
- (93) Kauzlarich, S. M.; et al. Structure and high-temperature thermoelectric properties of SrAl<sub>2</sub>Si<sub>2</sub>. *J. Solid State Chem.* **2009**, *182*, 240–245.
- (94) Bocher, L.; et al. CaMn<sub>1-x</sub>Nb<sub>x</sub>O<sub>3</sub> (x $\leq$ 0.08) perovskite-type phases as promising new high-temperature n-type thermoelectric materials. *Inorganic chemistry* **2008**, *47*, 8077–8085.
- (95) Backhaus-Ricoult, M.; et al. Semiconducting large bandgap oxides as potential thermoelectric materials for high-temperature power generation? *Appl. Phys. A: Mater. Sci. Process.* **2014**, *116*, 433–470.
- (96) Kirkham, M. J.; et al. Abinitio determination of crystal structures of the thermoelectric material MgAgSb. *Phys. Rev. B* **2012**, *85*, 144120.
- (97) Çelik, F.; et al. Acetate based CaMnO<sub>3</sub> thermoelectric material synthesis: effects on efficiency, phase formation, and microstructural change. *International Journal of Environmental Science and Technology* **2023**, *20*, 13083.
- (98) Nan, B.; et al. Bottom-Up Synthesis of SnTe-Based Thermoelectric Composites. *ACS Appl. Mater. Interfaces* **2023**, *15*, 23380–23389.
- (99) Gross, O. Precious metal based bulk glass-forming liquids: Development, thermodynamics, kinetics and structure. *PhD Thesis*, 2018.

- (100) Dong, J.; et al. Lead-free MnTe mid-temperature thermoelectric materials: facile synthesis, p-type doping and transport properties. *Journal of Materials Chemistry C* **2018**, *6*, 4265–4272.
- (101) Fu, C.; et al. Realizing high figure of merit in heavy-band p-type half-Heusler thermoelectric materials. *Nat. Commun.* **2015**, *6*, 8144.
- (102) Xiong, D.-B.; Okamoto, N. L.; Inui, H. Enhanced thermoelectric figure of merit in p-type Ag-doped ZnSb nanostructured with Ag<sub>3</sub>Sb. *Scripta Materialia* **2013**, *69*, 397–400.
- (103) Yu, J.; et al. High performance p-type half-Heusler thermoelectric materials. *J. Phys. D: Appl. Phys.* **2018**, *51*, 113001.
- (104) Harman, T. C.; et al. Nanostructured thermoelectric materials. *Journal of electronic materials* **2005**, *34*, L19–L22.
- (105) Chen, C.-L.; et al. Thermoelectric properties of p-type polycrystalline SnSe doped with Ag. *Journal of Materials Chemistry A* **2014**, *2*, 11171–11176.
- (106) Peng, H.; Kioussis, N.; Snyder, G. J. Elemental tellurium as a chiral p-type thermoelectric material. *Phys. Rev. B* **2014**, *89*, 195206.
- (107) Yang, C.; et al. New stannite-like p-type thermoelectric material Cu<sub>3</sub>SbSe<sub>4</sub>. *J. Phys. D: Appl. Phys.* **2011**, *44*, 295404.
- (108) Singh, N. K.; et al. The effect of doping on thermoelectric performance of p-type SnSe: Promising thermoelectric material. *J. Alloys Compd.* **2016**, *668*, 152–158.
- (109) Pandey, T.; Peeters, F. M.; Milosevic, M. V. High thermoelectric figure of merit in p-type Mg<sub>3</sub>Si<sub>2</sub>Te<sub>6</sub>: Role of multi-valley bands and high anharmonicity. *Journal of Materials Chemistry C* **2023**, *11*, 11185–11194.
- (110) Yuan, D.; et al. Air-stable n-type thermoelectric materials enabled by organic diradicaloids. *Angew. Chem., Int. Ed.* **2019**, *58*, 4958–4962.
- (111) Yu, J.; Sun, Q. Bi<sub>2</sub>O<sub>2</sub>Se nanosheet: An excellent high-temperature n-type thermoelectric material. *Appl. Phys. Lett.* **2018**, DOI: 10.1063/1.5017217.
- (112) Zhang, J.; et al. New insight on tuning electrical transport properties via Chalcogen doping in n-type Mg<sub>3</sub>Sb<sub>2</sub>-based thermoelectric materials. *Adv. Energy Mater.* **2018**, *8*, 1702776.
- (113) Lu, Y.; Wang, J.-Y.; Pei, J. Strategies to enhance the conductivity of n-type polymer thermoelectric materials. *Chem. Mater.* **2019**, *31*, 6412–6423.
- (114) Meng, B.; Liu, J.; Wang, L. Recent development of n-type thermoelectric materials based on conjugated polymers. *Nano Materials Science* **2021**, *3*, 113–123.
- (115) Sun, Y.; Di, C.-A.; Xu, W.; Zhu, D.; et al. Advances in n-type organic thermoelectric materials and devices. *Adv. Electron. Mater.* **2019**, *5*, 1800825.
- (116) Nonoguchi, Y.; et al. Systematic conversion of single walled carbon nanotubes into n-type thermoelectric materials by molecular dopants. *Sci. Rep.* **2013**, *3*, 3344.
- (117) Zhang, J.; et al. Discovery of high-performance low-cost n-type Mg<sub>3</sub>Sb<sub>2</sub>-based thermoelectric materials with multi-valley conduction bands. *Nat. Commun.* **2017**, *8*, 13901.
- (118) Li, J.; et al. Defect chemistry for n-type doping of Mg<sub>3</sub>Sb<sub>2</sub>-based thermoelectric materials. *J. Phys. Chem. C* **2019**, *123*, 20781–20788.
- (119) Shi, Ke; et al. Toward high performance n-type thermoelectric materials by rational modification of BDPPV backbones. *J. Am. Chem. Soc.* **2015**, *137*, 6979–6982.
- (120) Yura, R.; et al. Crown ether salt-doped ladder-type conducting polymers for air-stable n-type thermoelectric materials. *Chem. Commun.* **2023**, *59*, 5531–5534.
- (121) Chen, Z.; et al. GaSb doping facilitates conduction band convergence and improves thermoelectric performance in n-type PbS. *Energy Environ. Sci.* **2023**, *16*, 1676–1684.
- (122) Huang, S.-Z.; et al. Strain Tunable Thermoelectric Material: Janus ZrSSe Monolayer. *Langmuir* **2023**, *39*, 2719–2728.
- (123) Mohammed, M. A.; et al. A review of thermoelectric p-type Ca<sub>3</sub>Co<sub>4</sub>O<sub>9</sub> nanostructured ceramics for exhaust energy recovery. *Conference: 2nd International Symposium on Engine Boosting and Energy Recovery*; 2017.
- (124) Zaia, E. W.; et al. Progress and perspective: soft thermoelectric materials for wearable and Internet-of-Things applications. *Adv. Electron. Mater.* **2019**, *5*, 1800823.
- (125) Huang, Y.; et al. Organic Cocrystals: Beyond Electrical Conductivities and Field-Effect Transistors (FETs). *Angew. Chem., Int. Ed.* **2019**, *58*, 9696–9711.
- (126) Lu, Y.; et al. The critical role of dopant cations in electrical conductivity and thermoelectric performance of n-doped polymers. *J. Am. Chem. Soc.* **2020**, *142*, 15340–15348.
- (127) Zhang, F.; et al. Flexible and self-powered temperature–pressure dual-parameter sensors using microstructure-frame-supported organic thermoelectric materials. *Nat. Commun.* **2015**, *6*, 8356.
- (128) Deng, J.; et al. Vitrimer elastomer-based jigsaw puzzle-like healable triboelectric nanogenerator for self-powered wearable electronics. *Adv. Mater.* **2018**, *30*, 1705918.
- (129) Russ, B.; et al. Organic thermoelectric materials for energy harvesting and temperature control. *Nat. Rev. Mater.* **2016**, *1*, 1–14.
- (130) Lee, L.-H. All one needs to know about metaverse: A complete survey on technological singularity, virtual ecosystem, and research agenda. *arXiv preprint arXiv:2110.05352* **2021**.
- (131) Chander, M.; et al. Organic livestock production: an emerging opportunity with new challenges for producers in tropical countries. *Rev. sci. tech. Off. int. Epiz* **2011**, *30*, 569–583.
- (132) Sen, S.; Patil, S.; Argyropoulos, D. S. Thermal properties of lignin in copolymers, blends, and composites: a review. *Green Chem.* **2015**, *17*, 4862–4887.
- (133) Zhu, T.; et al. Compromise and synergy in high-efficiency thermoelectric materials. *Advanced materials* **2017**, *29*, 1605884.
- (134) Tan, G.; Li-Dong, Z.; Kanatzidis, M. G. Rationally designing high-performance bulk thermoelectric materials. *Chem. Rev.* **2016**, *116*, 12123–12149.
- (135) Chen, Y.; Zhao, Y.; Liang, Z. Solution processed organic thermoelectrics: towards flexible thermoelectric modules. *Energy Environ. Sci.* **2015**, *8*, 401–422.
- (136) Lindorf, M.; et al. Organic-based thermoelectrics. *Journal of materials chemistry A* **2020**, *8*, 7495–7507.
- (137) Meng, Y. S.; Arroyo-de Dompablo, M. E. First principles computational materials design for energy storage materials in lithium ion batteries. *Energy Environ. Sci.* **2009**, *2*, 589–609.
- (138) Babudri, F.; Farinola, G. M.; Naso, F.; Ragni, R.; et al. Fluorinated organic materials for electronic and optoelectronic applications: the role of the fluorine atom. *Chem. Commun.* **2007**, *10*, 1003–1022.
- (139) Wu, Z.; et al. Thermoelectric converter: Strategies from materials to device application. *Nano Energy* **2022**, *91*, 106692.
- (140) Wudil, Y. S.; et al. The multi-dimensional approach to synergistically improve the performance of inorganic thermoelectric materials: A critical review. *Arabian Journal of Chemistry* **2021**, *14*, 103103.
- (141) Song, P.; et al. Fabrication of exfoliated graphene-based polypropylene nanocomposites with enhanced mechanical and thermal properties. *Polymer* **2011**, *52*, 4001–4010.
- (142) Singh, D.; Ahuja, R. Dimensionality effects in high-performance thermoelectric materials: Computational and experimental progress in energy harvesting applications. *Wiley Interdisciplinary Reviews: Computational Molecular Science* **2022**, *12*, No. e1547.
- (143) Schierning, G.; et al. Concepts for medium-high to high temperature thermoelectric heat-to-electricity conversion: a review of selected materials and basic considerations of module design. *Translational Materials Research* **2015**, *2*, 025001.
- (144) Ammar, Y.; et al. Low grade thermal energy sources and uses from the process industry in the UK. *Applied Energy* **2012**, *89*, 3–20.
- (145) Zeng, M.; et al. Printing thermoelectric inks toward next-generation energy and thermal devices. *Chem. Soc. Rev.* **2022**, *51*, 485–512.